

# X-ray view of Dissipative Warm Corona in AGN

B. Palit<sup>1</sup>, A. Różańska<sup>1</sup>, P. O. Petrucci<sup>2</sup>, D. Gronkiewicz<sup>1</sup>, S. Barnier<sup>6</sup>, S. Bianchi<sup>4</sup>, D. R. Ballantyne<sup>5</sup>, V. E. Gianolli<sup>2,4</sup>, R. Middei<sup>7,8</sup>, R. Belmont<sup>3</sup>, and F. Ursini<sup>2</sup>

<sup>1</sup> Nicolaus Copernicus Astronomical Center, Polish Academy of Sciences, Bartycka 18, 00-716 Warsaw, Poland

<sup>2</sup> Université de Grenoble Alpes, IPAG, F-38000 Grenoble, France

<sup>3</sup> Université Paris Cité, Université Paris-Saclay, CEA, CNRS, AIM, F-91191, Gif-sur-Yvette, France

<sup>4</sup> Dipartimento di Matematica e Fisica, Università degli Studi Roma Tre, via della Vasca Navale 84, I-00146 Roma, Italy

<sup>5</sup> Center for Relativistic Astrophysics, School of Physics, Georgia Institute of Technology, 837 State Street, Atlanta, GA 30332-0430, USA

<sup>6</sup> Theoretical Astrophysics, Department of Earth and Space Science, Graduate School of Science, Osaka University, Toyonaka, Osaka 560-0043, Japan

<sup>7</sup> Space Science Data Center, Agenzia Spaziale Italiana, Via del Politecnico snc, 00133 Roma, Italy

<sup>8</sup> INAF Osservatorio Astronomico di Roma, Via Frascati 33, 00078 Monte Porzio Catone (RM), Italy

Received September 15, 0001; accepted March 16, 1997

## ABSTRACT

*Context.* In the X-ray spectra of active galactic nuclei (AGNs), a noticeable excess of soft X-rays is typically detected beyond the extrapolation of the power-law trend observed between 2 and 10 keV. The cause of this surplus remains unclear. In the scenario of warm Comptonization, observations propose a warm corona temperature ranging from 0.1 to 1 keV and an optical depth of approximately 10 to 20. Furthermore, according to radiative constraints derived from spectral analyses employing Comptonization models, it is suggested that the majority of the accretion power is released within the warm corona, while the disk beneath it is largely non-dissipative, emitting mainly the reprocessed radiation from the corona.

*Aims.* We test the dissipative warm corona model using the radiative transfer code- TITAN/NOAR on a sample of 82 *XMM-Newton* EPIC-pn observations of AGNs. Through spectral modeling of the X-ray data, we aim to estimate the total amount of internal heating inside the warm corona situated on top of the accretion disk.

*Methods.* By modeling the 0.3–10 keV EPIC-pn spectra with the TITAN/NOAR model component we estimate the internal heating and optical depth of the warm corona and check their correlations with global parameters such as: hot corona spectral index, black hole mass and accretion rate. From model normalization, we compute the radial extent of warm corona on top of cold accretion disk.

*Results.* Our model infers the presence of dissipative warm corona, with optical depths distributed in the range  $\sim 6$ –30 and total internal heating in the range  $\sim 1$ –29  $\times 10^{-23}$  erg s<sup>-1</sup> cm<sup>3</sup>. We do not detect any variation of these properties with global properties like black hole mass and accretion rate. The extent of warm corona is spread across a large range from 7–408 gravitational radii, and we find that warm corona is more extended for larger accretion rates.

*Conclusions.* Soft excess emission is ubiquitous in AGNs across wide mass range and accretion rate. We confirm that warm corona responsible for producing the soft-excess is highly dissipative in nature with larger optical depths being associated with lower internal heating and vice versa. The presence of cold standard accretion disk regulates the extent of warm corona.

**Key words.** X-rays: galaxies – Methods: observational – Galaxies: active – Galaxies: Seyfert

## 1. Introduction

Despite major advancements in understanding the X-ray spectral features of Active Galactic Nuclei (AGNs), the origin of soft X-ray excess (Pravdo et al. 1981) still baffles the community. Typically the X-ray spectra of Seyfert 1 galaxies are dominated by primary emission in the form of hard X-ray power law above 2 keV. This originates in the hot, optically thin plasma close to the central black hole. When the hard power law is extrapolated below 2 keV, a smooth excess rises above it, which is known as the soft X-ray excess.

Generally well described by a comptonized emission, the electron temperature of ‘soft-excess’ peaks at  $\sim 0.1$  - 0.5 keV for a diverse range of AGNs (Czerny et al. 2003; Done et al. 2012). Such constancy of temperature points towards a similar origin of

emission in different types of AGN, which may be connected with reprocessing of the X-ray emission. This resulted in associating either blurred reflection (Fabian et al. 2004; Crummy et al. 2006) or blurred ionized wind absorption (Gierliński & Done 2004) as probable origins of the soft-excess. In case of the blurred ionized disk reflection model, intrinsic hard X-rays are focused on the accretion disk producing reflection continuum with a dense forest of emission lines which are then relativistically broadened due to close proximity to the supermassive black hole (SMBH). While it nicely reproduces the smooth shape of soft-excess and also demonstrates a physical connection with spectral turnover at  $\sim 30$  keV (known as the Compton reflection hump), it is expected that soft-excess strength must correlate with strength of reflection. However, the opposite relation was observed by Boissay et al. (2016), who determined that reflection factor anti-correlates with the strength of the soft-excess in the sample of about 102 sources. In addition, the high spin of black hole required and high disk

Send offprint requests to: B. Palit

\* E-mail: bpalit@camk.edu.pl (BP)

density ( $\geq 10^{18} \text{ cm}^{-3}$ ) inferred from the model raise questions about its feasibility. The same conclusion ended the smeared absorption model, which requires a very high speed of an ionized wind, up to around  $0.9c$  to provide sufficient relativistic blurring to fit the spectra correctly (Schurch & Done 2008).

One plausible way to connect soft-excess with atomic data is the model of Compton reflection from a purely hydrogen atmosphere found by Madej & Rózańska (2000), where authors demonstrated, that Compton scattering can shift high energy photons toward lower energies during reflection from fully ionized matter consisting of hydrogen only. The soft-excess arises when the lack of heavy elements prevents absorption of soft photons re-emitted in the process of Compton down-scattering. Nevertheless, this result was unexplored further due to its complexity, and X-ray data invoked simpler phenomenological solutions. To match the hard energy tail of the soft-excess, an additional Comptonization component can be used while fitting the data (Magdziarz et al. 1998; Mehdipour et al. 2011; Jin et al. 2012; Petrucci et al. 2013, 2018; Porquet et al. 2018; Tripathi et al. 2021, and references therein). This led to the argument that soft-excess could also arise from a separate Comptonizing medium, where a warm (electron temperature  $kT_e \sim 0.1 - 0.5 \text{ keV}$ ), optically thick (optical depth  $\tau > 1$ ) corona (distinct from the hot optically thin corona) is responsible for Compton up-scattering of seed photons from the disk (optical/UV energy range) and producing the characteristic shape of soft-excess (Magdziarz et al. 1998; Done et al. 2012; Petrucci et al. 2013). This additional Comptonized layer, referred to as the warm corona, may be considered as a radial zone separate from standard disk (Done et al. 2012; Kubota & Done 2018) or a warm optically thick layer on top of the standard disk (Janiuk et al. 2001; Rózańska et al. 2015; Gronkiewicz et al. 2023). Correlation found between UV/X-ray strongly support this interpretation (Mehdipour et al. 2011; Noda et al. 2011, 2013; Petrucci et al. 2013; Gliozzi & Williams 2020). Most of the models fitted to observations are phenomenological in nature and lack physical grounds for origin of such warm layer. Furthermore, with the data in the energy range provided by most missions, that is, 0.3–10 keV, is well suited to study the soft X-ray excess. However, it is not possible to differentiate the reflection model from the warm Comptonization model, based on spectral fitting (García et al. 2019). Only simultaneous *XMM-Newton* and *NuSTAR* observations (0.3–79 keV) may provide those information, but such data are still not available for many sources. In this paper, we focus on the *XMM-Newton* EPIC-pn data which has high effective area in the 0.3–2 keV in order to study soft X-ray excess.

Application of the warm Comptonization model on extensive X-ray observations yielded the presence of an optically thick layer of depth 10–20 and temperature  $\sim 1.0 \text{ keV}$  (Magdziarz et al. 1998; Page et al. 2004; Mehdipour et al. 2011; Jin et al. 2012; Petrucci et al. 2013; Matt et al. 2014; Mehdipour et al. 2015; Porquet et al. 2018; Ursini et al. 2018; Middei et al. 2018, 2019a). By modeling the energy balance between warm corona and cold disk, it was proven by Rózańska et al. (2015) that such warm corona, cooled by Comptonization, has to be additionally heated by some internal process, most probably mechanical heating, in order to stay in hydrostatic equilibrium with cold accretion disk. Furthermore, it was suggested that existence of magnetic pressure or mass outflow was required to stabilize the warm corona of optical depth larger than 5. The above consideration did not specify any particular heating, it only showed that corona must dissipate energy to be constantly visible, as observed in Mrk 509 (Petrucci et al. 2013).

On the other hand, it was pointed out by García et al. (2019), that the emergent spectra from optically thick layer should carry strong signatures of absorption lines in soft X-ray spectrum which contradicts the smooth shape of soft-excess. However, when theoretical models of warm corona emission were computed including additional mechanical heating of plasma, the modeled spectra appeared featureless, in agreement with observations (Petrucci et al. 2020; Xiang et al. 2022). Most probably excess heating raises the ionization state of matter in the optically thick warm corona, in turn reducing the photo-electric opacity. This smoothens the absorption features. Then, a new question arises: what is the physical justification of the energy dissipation in the warm corona, and can we estimate the amount of warm corona heating from observations?

Recently, a follow-up of Optical/UV continuum emission was seen to track the changes in soft-excess, suggesting a link between intrinsic disk emission and its interaction with warm corona producing the soft-excess (Mehdipour et al. 2023). Such findings confirm our model of the dissipative flow, where both vertical layers: warm corona and cold disk, are heated by magneto-rotational instability (MRI) and radiatively coupled (Gronkiewicz et al. 2023). Such additional heating ensures that scattering dominates over photoelectric absorption, hence smoothing sharp features in the emergent spectra. However, the above model only shows that warm corona and cold disk layer can coexist in equilibrium, both self-consistently heated by MRI according to the scheme proposed by Begelman et al. (2015), where the transition between layers is justified by stating global boundary conditions. To produce the spectra for data fitting, advanced radiative transfer codes should be used. Current codes cannot self-consistently produce dissipative warm corona coupled with an accretion disk. They only include additional heating in the energy balance equation of the warm layer cooled by the Comptonization of soft photons. Such spectral models became recently available with the *reXcor* model (Xiang et al. 2022) and by the *TITAN/NOAR* code (Petrucci et al. 2020), where the former model was tested with real data (Porquet et al. 2024; Ballantyne et al. 2024), but the later only very recently, for one source HE1029-1401 (Vaia et al. 2024).

In this work, we test a new dissipative warm corona emission model computed by radiative transfer code *TITAN/NOAR* (Petrucci et al. 2020), with a sample of 21 AGN observed with the *XMM-Newton* satellite over last two decades. In total, 82 observations have been analyzed in this paper, thus allowing to put observational constraints on the amount of internal heating required by warm corona to sustain hydrostatic equilibrium with cold accretion disk. The main assumptions of warm, dissipative corona in our model together with comparison with *reXcor* model are present in Sect. 2, including the approach of numerical computations of the soft-excess emission. In Sect. 3 we outline about our AGN sample. In Sect. 4 we elaborate on the total model considered in data fitting process. Results are interpreted in Sect. 5 before drawing final conclusion in Sect. 6.

## 2. General model assumptions

A toy model describing different emission components contributing to the total X-ray spectra is shown in Fig. 1. We consider only radio quiet sources, with negligible jet emission. Therefore, all observed X-ray emission originates from the inner accretion flow, that can have multi-phase nature. Inner accretion flow geometry is often described using a stratified model consisting of two separate regions of plasma, one nearest to black hole is the hot corona (shown in red) and next to the hot corona the second zone lying on the top of a cold accretion disk named the

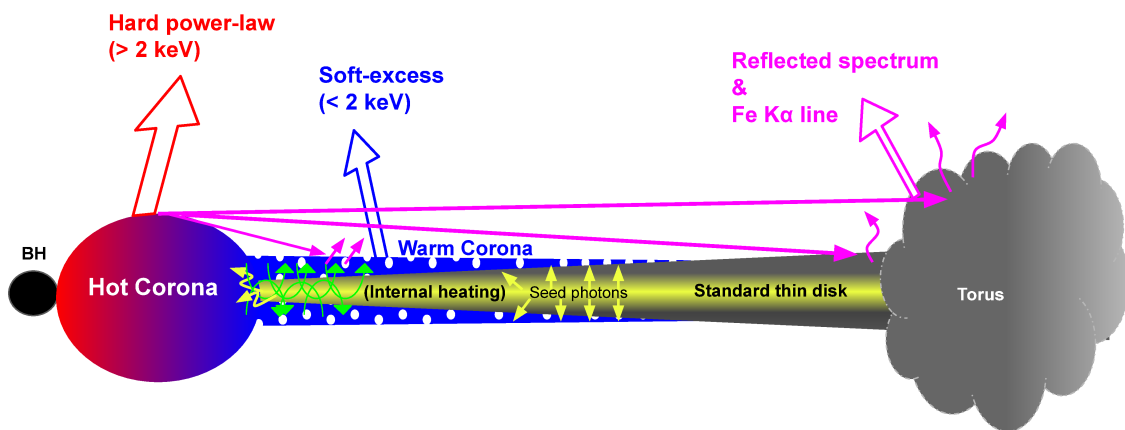


Fig. 1: Different emitting components considered in our data analysis of AGN hosting black hole in its center. Inner hot corona (red) is responsible for continuum emission above 2 keV in the form of power-law. Hard X-ray radiation illuminates each part of the inner disk and the reflection is self consistently computed by our code TITAN/NOAR. Reflected emission (magenta) can originate from the outer disk (yellow) as well as from the distant torus (grey). The two-phase slab of warm corona (blue) and cold disk (yellow) is responsible for producing soft-excess emission by up-scattering UV/optical seed photons from the disk. Additional internal heating in this region assumed in our model is marked with curved green arrows.

warm corona (in blue) forming the so called sandwich geometry (Haardt & Maraschi 1993). The warm corona is optically thick and is cooled in the process of up-scattering soft-seed photons from the standard disk. It is believed to produce the soft X-ray excess which is seen in the energy range 0.1 - 2 keV. The transition radius between single-phase hot flow and two-phase warm corona coupled with cold disk is not known, but to make it possible we should specify the physical process responsible for such transition. Past research focused on the disk evaporation model as a smooth change between cold accretion flow and hot corona (Rózańska & Czerny 2000a,b), but this model still needs further theoretical exploration.

This paper is an attempt to study warm corona in terms of the amount of energy dissipated in this layer situated on the top of a cold disk. The outgoing spectrum is calculated with radiative transfer code TITAN (Dumont et al. 2003), which fully solves the transfer of radiation through the stratified matter with heavy elements, taking into account additional mechanical heating in energy balance to justify temperature equilibrium. Simultaneously, an ionization balance in non-local thermal equilibrium (non-LTE) regime, and Compton scattering are fully taken into account with Monte Carlo procedure named NOAR (Dumont et al. 2000; Abrassart & Dumont 2001). Non-LTE regime means that full statistical equation of state for ionization balance is solved during numerical computations of models, and all bound-free and bound-bound processes are taken into account together with free-free absorption and scattering. Petrucci et al. (2020) demonstrated that the models of dissipative warm corona computed by TITAN/NOAR code can fully reproduce the temperature stratification inside warm corona and outgoing spectral shape in agreement with what is generally observed. For the first time we test TITAN/NOAR models with observations in order to determine the amount of energy which dissipates in the warm corona. Once we know, how much the warm corona is heated, we will be able to propose physical mechanism responsible for the heating the plasma to the temperatures visible in X-rays.

There is already a model of soft-excess available for data fitting, named `reXcor`, which considers emission from dissipative warm corona computed with full transfer of radiation through ionized skin (Ballantyne 2020), but it is calculated for lamp-post

geometry, where intrinsic hard X-rays are produced in the point source above the black hole so that they illuminate a large portion of the innermost disk region (Nayakshin 2000). Then, X-ray illumination of the outer disk layers is reflected, and both: radiative heating by photoionization and constant internal heating interplay with each other. Relativistic corrections on illuminating radiation and outgoing emission are taken into account during final integration over disk surface. The global energy balance is achieved by assuming distribution of dissipated energy between: point source, warm corona and cold disk. In our case, the energy balance is calculated locally only between warm corona and cold disk. Therefore, our model is not tightly bounded with accretion rate and black hole mass, and purely estimates the amount of energy dissipated in warm corona. Full radiative transfer through the warm corona is computed together with reflection, but since the warm corona is optically thick, the outgoing emission is devoid of reflection signatures, and our computed model represents only separate model component responsible for soft-excess ready to use in data fitting packages (e.g., XSPEC).

### 2.1. Energy dissipation in the warm corona

Given that the radiative heating is not enough to produce optically thick, warm layer on the top of an accretion disk (Rózańska et al. 2015), we consider that, in addition to external illumination, warm corona is also internally heated that is, the part of energy generated in accretion process is dissipated in the layer. The example of such heating was considered in the past (Gronkiewicz & Rózańska 2020; Gronkiewicz et al. 2023) in the form of heating by magneto rotational instability (MRI), but it was never coupled with spectral calculations. Therefore, in the model presented here, we do not specify the origin of this internal heating. However, we assume here that the input energy rate in a warm corona, per unit optical depth and solid angle,  $Q$  is uniform, and it corresponds to the flux emitted by warm corona toward observer.

$$F_{\text{cor}} = 4\pi\tau_{\text{cor}}Q, \quad (1)$$

where  $\tau_{\text{cor}}$  is optical depth of the warm corona, which is an input parameter in our numerical calculations. Therefore, total

mechanical heating per particle per unit volume is:

$$q_h = \frac{4\pi\sigma_T Q}{n_H}, \quad (2)$$

where  $\sigma_T$  is a Thomson cross section, and  $n_H$  is hydrogen density number of the gas. This quantity, after multiplying by electron and proton density number, that is,  $n_H n_e q_h$  in  $\text{erg s}^{-1} \text{cm}^{-3}$  is an input parameter into radiative transfer TITAN code.

At each stage of our considerations we ensure that the energy balance between warm corona and cold disk is sustained, that is, total energy deposited via accretion process is divided between two layers. Taking into account that such energy is converted into radiation (with radiative energy for standard thin disk) and including reprocessing we get:

$$F_{\text{tot}} = F_{\text{cor}} + F_{\text{int}}, \quad (3)$$

where,  $B$  is the frequency integrated black-body radiation intensity, so  $F_{\text{int}}$  is sum of intrinsic emission from disk due to thermalized black-body  $4\pi B/(4 + 3\tau_{\text{cor}})$  and reprocessed emission  $2\pi\tau_{\text{cor}}Q$ , coming from base of corona (Róžańska et al. 2015; Petrucci et al. 2020). The above fluxes are needed to estimate the fraction of energy dissipated in the corona relative to the total energy dissipation,  $\chi$  (not to be confused with goodness of fit  $\chi_{\text{red}}^2$ ), which can be derived while fitting numerical models to observations:

$$\chi = \frac{F_{\text{cor}}}{F_{\text{tot}}} = \frac{\tau_{\text{cor}} n_H q_h}{\sigma_T F_{\text{tot}}}. \quad (4)$$

Even though, we here use different symbols, the internal heating of the warm corona is defined in the same way as in reXcor model. Our  $\chi$  corresponds to  $h_f$  in Eq. 7 of Xiang et al. (2022) paper, and our  $q_h$  is simply  $\mathcal{H}$  of that paper. The only difference is, that in reXcor model, total energy deposited by accretion is divided into three emitting areas: point X-ray source (lampost model), warm corona and cold disk, while in our paper, it is divided between warm corona and cold disk. Therefore, even if our models have different overall geometry connected to external X-ray source, (i.e., lampost versus hot inner corona model) the idea of dissipative corona above an accretion disk is the same, and we can directly compare our results. Quantitatively, we have to keep in mind, that the dissipation fraction defined in our model relates to the disk black body radiation intensity and warm corona intensity as:

$$\chi = \frac{\tau_{\text{cor}} Q}{\frac{B}{4+3\tau_{\text{cor}}} + \frac{\tau_{\text{cor}} Q}{2}}. \quad (5)$$

The total energy flux  $F_{\text{tot}}$  generated by accretion process, directly relates to accretion rate by standard formulae, for which we assume an accretion efficiency parameter. Because accretion efficiency has long been a topic of discussion among theoreticians and observers alike, for our work here, we do not tie this flux to particular value of an accretion rate. The aim of our research is to find observational constrains on the amount of energy released in the warm corona by additional heating. For this purpose we use radiative transfer code TITAN, which has the possibility to include different strengths of illuminating continuum for both sides of the slab and internal heating of the gas. The connection of the observed flux to eventual accretion rate of the source also comes from observations, and we discuss this issue below in this paper.

## 2.2. TITAN and NOAR spectral models

The full description of the procedure of spectral model preparation is given in Petrucci et al. (2020). In this paper, we use those models of warm, dissipative corona to fit observations of AGN sample described in 3. The grid of models was computed with the radiative transfer code TITAN (Dumont et al. 2003) coupled with Monte-Carlo code NOAR, where the former accounts for ionization and thermal equilibrium of the gas, and the later for detailed treatment of Comptonization. The iteration between both codes undergoes up to convergence and the final angle-dependent spectrum accounts for external X-ray illumination from the top, reflection on the illuminated side, transmission through the gas, illumination by seed photons from the bottom, and additional internal heating constant over gas volume. During the computations all free-free, bound-free, and bound-bound atomic processes are taken into account allowing to transfer continuum radiation and lines. The coupling between TITAN and NOAR allows a complete treatment of the emission from a photoionized, Comptonized medium and can be used in a variety of cases, as illuminated disk atmospheres (Róžańska et al. 2002) and warm absorbers (Róžańska et al. 2006) in AGN. For our work here, TITAN/NOAR models corresponding to the emission from the warm corona are denoted by blue empty arrow in Fig. 1.

We compute spectra for a large range of parameters: gas density number –  $n_H$ , warm corona optical depth –  $\tau_{\text{cor}}$ , dissipation rate –  $q_h$ , ionization parameter as the normalization for power-law shaped external X-rays illuminating the surface of the warm corona –  $\xi$ , power-law spectral index of illuminated continuum –  $\Gamma$ , power-law low and high energy cut-offs –  $h\nu_{\text{min}}$  and  $h\nu_{\text{max}}$ , and the temperature of soft photons injected into the bottom of warm corona, mimicking the disk black body emission –  $kT_{\text{bb}}$ . Since our goal is to put constrains on the amount of internal heating of the warm corona, the outcome of radiative transfer calculations is used to build spectral component that reflects warm corona emission only. We do not aim to fit reflection, and hot corona emission with TITAN/NOAR models. Therefore, for the purpose of data fitting in this paper, we have chosen to keep certain parameter values fixed:  $kT_{\text{bb}} = 7$  eV,  $\log \xi = 3$ ,  $\Gamma = 1.8$ , and  $n_H = 10^{12} \text{cm}^{-3}$ ,  $h\nu_{\text{min}} = 50$  eV and  $h\nu_{\text{max}} = 100$  keV, and free only the warm corona parameters, while building table models. These values are typical for supermassive black holes (Rees 1984) such as AGNs with black hole mass of  $10^8 M_{\odot}$ .

The gas density of the warm corona is strongly justified by the model of dissipative, magnetically supported corona above an accretion disk given by Gronkiewicz et al. (2023). The model does not solve energy dependent radiative transfer, and for this reason it cannot justify the first three parameters, that are kept fixed. While spectral index and ionization parameter are taken from many previous observational tests, the value of the seed photons temperature is not obvious. Such seed photons, are Comptonized in both hot and warm corona, and are responsible for final spectral shape of the warm corona. With the use of a thermal Comptonization model NTHCOMP (Zdziarski et al. 1996; Życki et al. 1999) available in X-ray fitting package XSPEC (Arnaud 1996) in Fig. 2 we show how the final Comptonized spectra depends on the seed photon temperature. Clearly, below the seed photon temperature  $kT_{\text{bb}} = 20$  eV, the shape of output spectra is less sensitive to  $kT_{\text{bb}}$ . This limit is equal to the maximum value of  $kT_{\text{bb}}$  obtained from spectral fitting X-ray/UV data in Petrucci et al. (2018). Hence, it justifies our choice of 7 eV for this parameter in the model.

With the above assumptions we are left with only two free parameters, that are warm corona optical depth  $\tau_{\text{cor}}$  and inter-

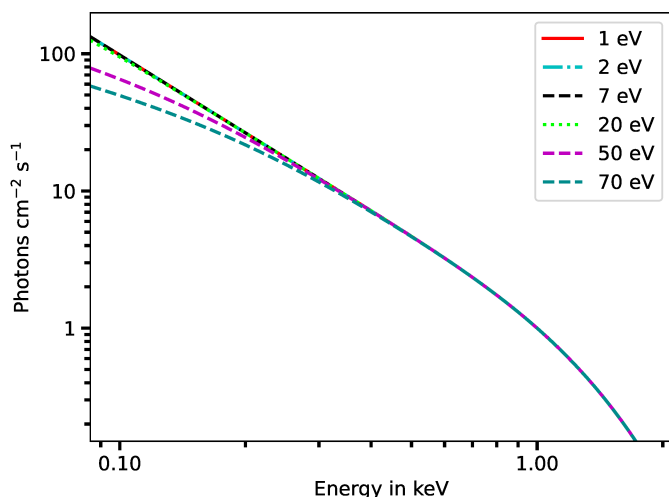


Fig. 2: The dependence of thermal Comptonization computed by NTHCOMP model (see Sect. 2.2 for discussion) on different values of input seed photon temperature ( $kT_{\text{bb}}$ ) ranging from 1 to 70 eV. Below  $kT_{\text{bb}}=20$  eV, there is negligible effect on the shape of Comptonized spectrum.

nal heating of the warm corona  $q_{\text{h}}$ . These parameters vary in the ranges of [5-30] and [ $10^{-23}$ - $10^{-21.5}$ ]  $\text{erg s}^{-1} \text{cm}^3$  while computing our grid of 196 soft-excess models, used below in the data fitting procedure. All TITAN/NOAR models are normalized to the case where the warm corona radius is  $10 R_{\text{g}}$ , and the distance to the source is equaled to 10 kpc, marked as  $D_{10}$ .  $R_{\text{g}}$  denotes the gravitational radius defined as  $R_{\text{g}}=GM_{\text{BH}}/c^2$ , where  $G$  is the gravitational constant,  $M_{\text{BH}}$  is a black hole mass, and  $c$  - the velocity of light. This means that for a typical black hole mass of  $10^8 M_{\odot}$ , all spectra are diluted by a factor of  $(10R_{\text{g}})^2/4\pi D_{10}^2 = 1.82 \times 10^{-18}$ . However, in our analysis, we kept the normalization of TITAN/NOAR model free during fitting process. In that case, it is interpreted as surface area of the soft-excess emitting warm corona. Taking the distance to the source  $D$  in units of  $D_{10}$  they are related as  $N_{\text{SE}} = S/D^2$ . Thus, assuming a spherically symmetric emitting area, we can estimate the size of warm emitting region by solving the equation:

$$R_{\text{cor}} = \sqrt{N_{\text{SE}} D^2 (10R_{\text{g}})^2 / \pi}, \quad (6)$$

with appropriate  $R_{\text{g}}$  value, calculated using black hole masses from Table 1.

### 3. Sample selection & Data reduction

Our AGN sample, drawn from Petrucci et al. (2018, hereafter P18), consisted of 21 nearby AGNs ( $z = 0.009$ – $0.5725$ ) that have been extensively observed by *XMM-Newton* X-ray telescope. There were a total of 14 type 1 Seyferts, 6 intermediate type Seyferts and one quasi stellar object (QSO). In total, 82 observations were analyzed and are listed in Table 1, where we also report their activity type, redshift, Galactic absorption and black hole mass, all taken from previous studies (P18).

One extra source- NGC 7469 was included in the parent sample. NGC 7469 is a luminous ( $L_{\text{Bol}}=10^{45} \text{ erg s}^{-1}$ , Behar et al. 2017a) nearby ( $z=0.0162$ ) Sy1 galaxy having strong soft-excess and narrow, neutral  $\text{FeK}\alpha$  and  $\text{FeK}\beta$  line components. It has been the subject of several multi-wavelength studies which led to detection of correlated UV/X-ray variability (Kumari et al. 2023)

Table 1: Sample of 21 AGNs studied in this paper

Source name	Seyfert activity type	Redshift $z$	$N_{\text{H}}^{\text{Gal}} \times 10^{20}$ [ $\text{cm}^{-2}$ ]	$\log M_{\text{BH}}$ [ $M_{\odot}$ ]
1H0419-577	1.5	0.1040	1.31	8.58
ESO198-G24	1.0	0.0455	3.26	8.48
HB890405-123	1.2	0.5725	4.16	-
HE1029-1401	1.2	0.0858	6.28	8.73
IRASF12397+3333	1.0	0.0435	1.31	6.66
LBQS1228+1116	QSO	0.2362	2.60	-
MRK 279	1.0	0.0304	1.59	7.54
MRK 335	1.0	0.0257	4.09	7.15
MRK 509	1.5	0.0343	5.16	8.16
MRK 590	1.0	0.0263	2.93	7.68
NGC 4593	1.0	0.009	2.05	6.28
NGC 7469	1.0	0.0162	5.24	7.04
PG0804+761	1.0	0.1000	3.51	8.24
PG0844+349	1.0	0.0640	3.22	7.97
PG1116+215	1.0	0.1765	1.46	8.53
PG1351+640	1.5	0.0882	2.10	7.66
PG1402+261	1.0	0.1640	1.44	7.94
PG1440+356	1.0	0.0790	1.08	7.47
Q0056-363	1.0	0.1641	1.94	8.95
RE1034+396	1.0	0.0424	1.36	6.41
UGC 3973	1.2	0.0221	6.61	7.72

#### Notes:

Redshifts are taken from NASA Extra-galactic Database- NED. Galactic column densities  $N_{\text{H}}^{\text{Gal}}$  are taken from Willingale et al. (2013).

The black hole masses are adopted from Petrucci et al. (2018) and see Bianchi et al. (2009) for detailed references.

and thermal outflows from AGN torus (Mehdipour et al. 2018). Furthermore, warm Comptonization scenario for the production of soft-excess has been repeatedly suggested for this source which makes it an ideal target for testing dissipative warm corona model.

The sources in our sample were simultaneously observed by *XMM-Newton* EPIC-pn camera (Strüder et al. 2001) along-with multiple Optical Monitor (OM) filters (Mason et al. 2001) with exposure times distributed between  $\sim 12$  and  $\sim 100$  ks. Since the disk black body temperature is fixed in our model, it was not possible to fit OM data and it was thus ignored.

For our analysis, we adopt the Eddington ratios ( $L_{\text{Bol}}/L_{\text{Edd}}$ ) derived in P18 and we report them in the third column of Table 3. For two sources HB890405-123 and LBQS1228+1116, the black hole mass was unavailable so the accretion rate was undetermined. As shown in Tabs. 1 and 3, the sources span a wide range of black hole masses as well as accretion rate. This ensures the possibility to detect any form of evolution of warm corona properties across masses. The data was reduced by P18 following the standard procedures of Science Analysis Software (Gabriel et al. 2004) guidelines. Also, we decided to omit the spectral data between 1.8–2.4 keV to avoid improper modeling of calibration uncertainties arising from detector quantum efficiency at the Si K-edge (1.84 keV) and mirror effective area at the Au M-edge ( $\sim 2.3$  keV) (Cappi et al. 2016a). For more details about data reduction, we refer the reader to P18 paper.

### 4. Warm Corona model in the AGN sample

All the data have been analyzed using the publicly available XSPEC package (Arnaud 1996), designed for spectral analysis

Table 2: The list of free and fixed parameters used in total model, which are crucial in data fitting process (see text for details).

Model Component	Parameters	
	Free	Fixed
TBABS	–	$N_{\text{H}}^{\text{Gal}}$
CLOUDY	$\xi_{\text{CL}}, N_{\text{H}}^{\text{CL}}$	$v_{\text{turb}} = 100 \text{ km s}^{-1}$
TITAN/NOAR	$q_{\text{h}}, \tau_{\text{cor}}, N_{\text{SE}}$	$kT_{\text{bb}} = 7 \text{ eV}, \log \xi = 3, \Gamma = 1.8$
NTHCOMP	$\Gamma_{\text{hc}}, N_{\text{hc}}$	$kT_{\text{hc}} = 100 \text{ keV}, kT_{\text{bb}}^{\text{hc}} = kT_{\text{bb}}$
XILLVER	$N_{\text{X}}$	$\Gamma_{\text{X}} = \Gamma_{\text{hc}}, E_{\text{c}} = 300 \text{ keV}, \xi_{\text{X}} = 1$
Sum	8	10 (2 pairs are tied)

in X-ray domain. In this section we formulate the total model used for the purpose of this paper.

The so called two-corona approach is most commonly described using dual Comptonization models, treating the hot and warm coronae as disjoint entities radially separated from each other. In the previous work (P18), authors fitted broadband UV/X-ray data using two Comptonization components, both being independently responsible for hot and warm corona emission. In their phenomenological approach, at first step the disk temperature was estimated by fitting data from all the available OM filters with the multi-color disk black body model DISKBB, taking into account the contributions from Broad Line Region & galaxy templates. Comptonized emission from warm and hot corona were modeled using the thermal Comptonization model, NTHCOMP (Zdziarski et al. 1996). The disk temperature-  $kT_{\text{bb}}$  estimated from OM part of data was fed into two NTHCOMP components as input for soft-seed photon temperature to describe soft-excess and hard continuum. The non-relativistic reflection model- XILLVER (García & Kallman 2010) was added to fit the Fe  $K\alpha$  line and any reflection component present. Finally, all those model components have been multiplied by warm absorber table model (for details see: Cappi et al. 2016b) computed with the use of publicly available CLOUDY code (Chatzikos et al. 2023, and references therein).

We take a similar approach, replacing one of the thermal Comptonization component responsible for soft-excess emission with the TITAN/NOAR warm corona emission model described in Sect. 2. The resulting total composite model is then:

$$\text{TBABS} \times \text{CLOUDY} \times (\text{TITAN/NOAR} + \text{NTHCOMP} + \text{XILLVER}), \quad (7)$$

where thermal Comptonization NTHCOMP model accounts for hot corona emission, and warm corona is described by TITAN/NOAR model. Apart from normalization  $N_{\text{SE}}$ , the TITAN/NOAR model has two free parameters: warm corona optical depth  $\tau_{\text{cor}}$ , and total internal heating  $q_{\text{h}}$ . The TITAN code computes temperature structure in the optically thick warm corona, so we do not get any singular estimate of warm corona temperature from our model. As described in Sect. 2, TITAN provides the value of internal heating of a warm layer existing on top of cold disk and also computes the optical depth of a warm corona, which is not given by NTHCOMP. Remaining parameters are kept the same as in P18. We fixed the temperature of hot corona  $kT_{\text{hc}} = 100 \text{ keV}$ , high energy cutoff ( $E_{\text{c}}$ ) of XILLVER illuminating continuum to 300 keV, and ionization parameter of this model to  $\log \xi_{\text{X}} = 0$ . Neutral Galactic absorption along a line-of sight was accounted by TBABS model where the  $N_{\text{H}}^{\text{Gal}}$  (consisting of contribution from

both ionized and molecular hydrogen) was frozen at the values that have been taken from Willingale et al. (2013) and are given in fourth column of Table 1. Following P18, the remaining residuals in the soft band were modeled with a warm absorber component given by CLOUDY table model. It has two free parameters: ionization parameter  $\xi_{\text{CL}}$  and column density  $N_{\text{H}}^{\text{CL}}$ . The turbulent velocity  $v_{\text{turb}}$  was fixed at  $100 \text{ km s}^{-1}$ .

In summary, there are 8 free parameters in the total model, including the normalization of additive model components,  $N_{\text{SE}}$ ,  $N_{\text{hc}}$  for hot corona, and  $N_{\text{X}}$  for reflection, all of them listed in Table 2. Among 12 fixed parameters, two pairs are tied, the seed photon temperature for hot and warm corona:  $kT_{\text{bb}}^{\text{hc}} = kT_{\text{bb}} = 7 \text{ eV}$ , and spectral index for hot corona and reflection:  $\Gamma_{\text{X}} = \Gamma_{\text{hc}}$ .

We are aware that model components resulting from radiative transfer computations, such as CLOUDY, XILLVER and TITAN depend on many other parameters, which are not commonly used in the fitting procedure. Therefore, we do not list them in the table. Nevertheless, we made sure they are in compliance, for instance, solar iron abundance and disk inclination ( $i = 30^\circ$ ) was assumed in XILLVER model. The choice of those parameters does not influence the main expected result of our analysis, that is an interplay between two model components, TITAN/NOAR and NTHCOMP responsible for soft-excess and hot corona emission, respectively. Also, we did not find a justification to use the relativistic reflection component instead of XILLVER model. Since the former has many more free parameters, it is prone to degeneracies, without improving the fit statistic considerably. We tested the effect of replacing XILLVER with relativistic model- RELXILL (García et al. 2013, 2014), on a prototypical source- 1H0419-577 and its impact on the warm corona is discussed in Appendix C. Overall, we found that relativistic reflection contributes mildly to soft-excess emission however with only EPIC-pn data it was not possible to constrain important physical parameters such as radius of inner accretion disk, iron abundance and spin of black hole. Adding RELXILL had negligible impact on warm corona properties. The non-relativistic reflection component used in our analysis, allows to fit the reflection features reasonably at the same time keeping the total model on the lowest level of complication. Therefore, we are able to make final conclusion on the properties of warm corona.

We developed an automatic fitting procedure to fit multiple observations. We use the object oriented Python interface to the XSPEC called PyXSPEC (Gordon & Arnaud 2021). Spectral files are read confining the energy range to 0.3 -10 keV and ignoring any ‘bad’ channels.

## 5. Results

### 5.1. Goodness of Fits

The final reduced chi-squared fit statistic  $\chi_{\text{red}}^2$  ( $\chi_{\text{stat}}^2/\text{d.o.f.}$  – per degrees of freedom) for each data set is presented in the second column of Table 3. In our analysis, 98% of the observations have  $\chi_{\text{red}}^2 < 1.5$ . A small number of fits converged to a very high reduced statistic and those data have been analyzed individually. In most cases, they were the ones with complex absorption below 2 keV. For instance, MRK 509, ObsID: 0601390801 required the addition of extra warm absorber, as well as freeing of the ionization parameter  $\xi_{\text{X}}$  of XILLVER model. It improved this particular data fit from 354.79/219 to 261.33/216 ( $\Delta\chi_{\text{stat}}^2 \sim 93$  for 3 extra d.o.f). A relative likelihood value of  $\sim 10^{-37}$  based on Akaike information criterion (AIC) indicates that the second model is much more likely to correctly describe the data.



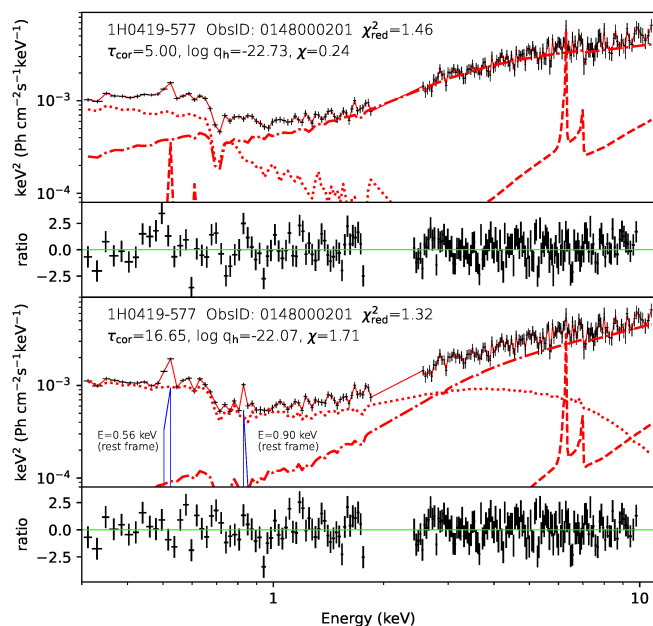


Fig. 3: Spectral model decomposition of 1H0419-577 data set with ObsID: 0148000201 fitted with our basic model given by Eq. 7 – upper panel, and the same model with two narrow Gaussians added - lower panel. By adding two narrow lines with fixed widths allowed to obtain a global minimum with relatively strong warm corona marked by dotted, red line. NTHCOMP component is presented by dotted-dashed red line, XILLVER is shown by dashed red line, while observations are given by black crosses. For each case, the ratio of data to folded model is plotted below.

Except for few sources with high value of column density, adding an extra warm absorber had negligible effect on the inferred optical depth, internal heating of warm corona and hard X-ray photon index. Four sources—(Mrk 509, RASF12397+3333, UGC 3973 and RE1034+396) required two warm absorbers to completely describe the complex features below 2 keV. Details of distribution of warm absorber column density and ionization level in our sample is discussed in Appendix A. Finally, in case of Mrk 335, the fit was greatly improved after adding a partial covering absorption model ZPCFABS (available in XSPEC) with  $\sim 90\%$  covering (see Longinotti et al. 2013), after leaving  $\xi_X$  free during fitting procedure (see Appendix D, Table D.1 for best fit values). The significant improvement in statistic is supported by a large change in  $\chi^2_{stat} \sim 250$  for 3 extra d.o.f and hence decrease in AIC value by 239.

To test the case of mild ionized reflection, we refitted all observations, keeping the ionization parameter of XILLVER unfrozen during the fit. Majority of sources turned out to have a neutral Fe K line, and in some cases the value of  $\xi_X$  could not be constrained. Unfreezing  $\xi_X$  did not have significant effect on other parameters, except that the parameter uncertainties were larger. Hence, we decided to keep it frozen to 1 for further discussion of final results.

Further, we had a closer look at the cases with reduced fit statistic higher than 1.3, checking the goodness of fit manually. We have found 11 data sets, attributed with 4 different sources: 1H0419-577, MRK335, NGC4593, and NGC7469 for which the resulting warm corona internal heating was noticeably low, close to the value of lower limit for this parameter. Checking the overall distribution of statistic for those cases, all of them displayed two

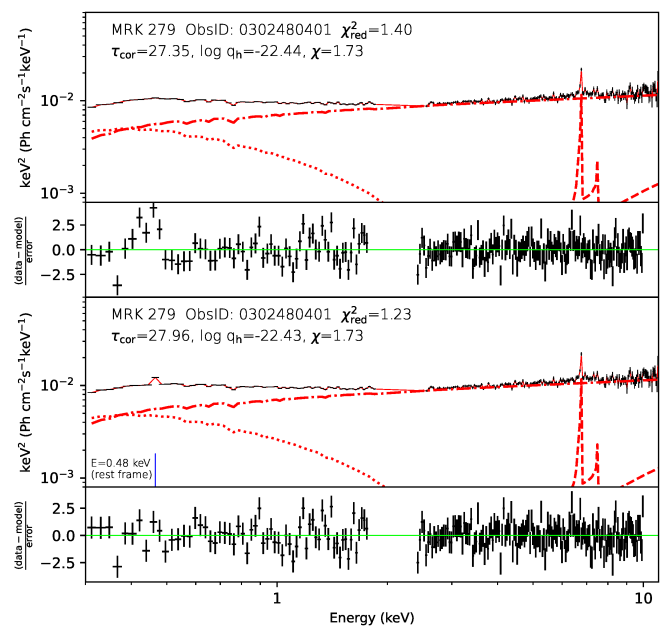


Fig. 4: Spectral model decomposition of MRK 279 data set with ObsID: 0302480401 fitted with our basic model given by Eq. 7 – upper panel, and the same model with one narrow Gaussian added - lower panel. By adding one narrow line allowed to improve fit statistic without affecting warm corona marked by dotted, red line. NTHCOMP component is presented by dotted-dashed red line, XILLVER is shown by dashed red line, while observations are given by black crosses. For each case, the ratio of data to folded model is plotted below.

local minima, one of them always located close to the edge of TITAN/NOAR parameter space. In addition, those cases exhibited narrow residuals at  $\sim 0.50 - 0.80$  keV. We refitted them using narrow Gaussians with width  $\sigma$  frozen at a limit of 1 eV, and energy centroid at roughly the peak value of sharp residual feature. Refitting those 11 data sets with additional one or two Gaussian narrow lines improved all fits in two ways: by lowering the reduced chi statistic, and removing local minimum located close to the limit of the parameter range. A better fit was found with noticeable change in warm corona parameters, and only minor change in other parameters. An example of such improvement is presented in Fig. 3, where the upper panel shows spectral decomposition of 1H0419-577 data (ObsID: 0148000201) fitted with our basic model given by Eq. 7, and lower panel shows the same model with two narrow Gaussians at energies 0.59 keV and 0.90 keV added, that caused the increase of warm corona heating  $\log q_h$  by 0.66 dex and  $\tau_{cor}$  from 5 to 16.65. Those lines were also detected in high resolution RGS (reflection grating spectrometer) data of this source and have been interpreted as O VII (0.56 keV) and Ne VII (0.90 keV) emission lines from narrow line region (NLR) (Di Gesu et al. 2013). Similar lines but with different identification have been reported in RGS spectra of NGC 4593 (Steenbrugge et al. 2003) and NGC 7469 (Behar et al. 2017b).

On the other hand, we had identified 10 different observations from 6 sources (1H0419-577, MRK335, NGC4593, NGC7469 and RE1034+396) for which by adding one or two narrow Gaussian lines of energies in ranges 0.48-0.56 keV and 0.70-0.90 keV helped to improve fit without affecting other model components. In recent works by Petrucci et al. (2018); Xu et al. (2021); Chalise et al. (2022); Ballantyne et al. (2024), the issue of resid-

uials in the CCD spectrum were tackled by adding such narrow Gaussians in the above energy ranges. Since CCD spectral resolution is incapable of resolving these emission lines, we made sure that their equivalent widths were below 10 eV, and they did not modify the soft excess continuum. In general, those features may correspond to the mixture of nitrogen, oxygen and iron lines originating from NLR as reported in the previous papers (Bianchi et al. 2006; Ebrero et al. 2010) and can be studied in detail with high resolution instruments ( $\sim 5$  eV) such as micro-calorimeters as X-IFU available with future mission ATHENA (Barret et al. 2023). As example, in Fig. 4 we show spectral decomposition of MRK 279 data (ObsID: 0302480401) without (upper panel) and with one Gaussian (bottom panel) added that allow us to improve fit statistic by 0.17 dex without a drastic change of warm corona parameters. Significance of the improvement in statistic was supported by a reduction of 37 units in AIC value. All above fit improvements are taken into account in Table 3 and in results presented below.

## 5.2. Properties of Warm Corona

Here we present the results of our data fitting procedure that is, the best fit model parameters, correlations between them, followed by interpretation of those results. The values of each data set fitted parameters are presented in Table 3. A list of remaining fit parameters is deferred to Appendix D. After fitting a self consistent model of warm, dissipative corona, cooled by Compton scattering, we constrained the internal heating responsible for the active, warm layer together with its optical depth. Subsequently, adopting Eq. 4, we compute the dissipation fraction of warm corona ( $\chi$  the values are listed in the eighth column of Table 3).

In the fourth column of Table 3, we present hardness ratio (HR), considering count rates and adopting the prescription: H (hard photon counts in range 2.0 - 10 keV), S (soft- photon counts 0.3 - 2 keV). Hardness ratio is calculated as:

$$HR = \frac{H - S}{H + S}. \quad (8)$$

We are aware that HR given as a ratio of measured counts, depends on the effective area of an instrument. *XMM-Newton* EPIC-pn has a higher effective area in the soft X-ray range compared to spectra above 2 keV which means that for the given similar flux level at both hard and soft energy ranges, the spectra will always be softer. Extreme values of HR may only be interpreted as truly hard or truly soft sources. Values in the middle are better described by spectral fitting. Due to constraints put on the hard powerlaw photon index, it is not directly indicative of strength of hot corona.

While the HR values computed in this work do not directly demonstrate any connection to the canonical states in X-ray binaries (XRBs) (Motta et al. 2009; Dunn et al. 2010), it does indicate at least qualitatively, whether the hot corona dominates over the warm corona and vice versa. Hence, it is a model independent way to capture the ‘state’ of inner accretion disk.

The total unabsorbed flux ( $F_{0.3-10}$ ) in the energy range 0.3–10 keV, was obtained by convolving the CFLUX XSPEC model with the group of additive components in our composite model given by Eq. 7. These fluxes were used to estimate the strength of soft-excess (SE) as:

$$SE = \frac{F_{0.3-2}(\text{CFLUX}*\text{TITAN}/\text{NOAR})}{F_{0.3-2}(\text{CFLUX}*\text{NTHCOMP})}. \quad (9)$$

It must be noted that multiplying a CLFUX does not affect the best fitted parameter values of the model. It merely scales the flux

array, calculated from all the components it acts upon, between the given energy points and returns the integrated flux with its error. The strength of soft-excess and total unabsorbed flux are listed in ninth and tenth column of Table 3 respectively.

We divided our sample into three groups based on the fitted values of hot corona photon index. Hard sources having  $\Gamma_{\text{hc}} < 1.70$ , intermediate – for  $1.70 < \Gamma_{\text{hc}} < 2.00$ , and soft – for sources with  $\Gamma_{\text{hc}} > 2.0$ . The total number of sources in these three categories are 41, 39 and 20, respectively. In Fig. 5, we also present statistical distribution of those three groups over warm corona fitted parameters. A significant fraction of observations in our sample agreed to moderately large optical depths of warm corona (Fig. 5, left), with a mean of  $\tau_{\text{cor}} = 18.26 \pm 0.12$ . In Fig. 5, (right) the internal heating of the warm corona  $\log q_{\text{h}}$  is also presented, and it shows two peaks around  $\log q_{\text{h}} \sim -22.50$  and  $\sim 22.00$ . The mean value of  $\log q_{\text{h}} = -22.25 \pm 0.03$ . Comparing it with the distribution of warm corona optical depth (on the left), we noticed that hard sources (blue dash-dotted line) are associated with warm corona having lower optical depth, but stronger internal heating. The inverse is seen in soft-sources (red solid line). Intermediate sources (green dashed line) have a wide spread in  $\tau_{\text{cor}}$  values but at slightly lower internal heating value.

Such behavior of warm corona properties with  $\Gamma_{\text{hc}}$  prompted us to check for correlations between warm corona parameters and spectral index of hard X-ray radiation as presented in Fig. 6 for all 82 observations. Each of the 21 sources are represented by markers of different style, referenced in the bottom right of Fig. 6. This convention is maintained throughout the paper. Markov Chain Monte Carlo (MCMC) simulations showing the distribution of Pearson’s r-values and p-values are presented in Appendix B.

As seen from Fig. 6 (b), based on all observations, we obtained a mild positive correlation between  $\tau_{\text{cor}}$  and hot corona spectral index  $\Gamma_{\text{hc}}$ , with Pearson’s rank correlation (r-value)  $0.38 \pm 0.06$ , which corresponded to  $\gg 99\%$  confidence level (see Appendix B for details). The grey dashed line at this figure indicate the best fit linear regression obtained using the bi-variate correlated errors and intrinsic scatter (BCES) technique (Akritas & Bershady 1996; Nemmen et al. 2012). We considered orthogonal least squares condition which treats both variables independently and also takes into account the effect of variable uncertainties. The equation of best fit line is represented as  $\tau_{\text{cor}} = (48.70 \pm 11.63) \Gamma_{\text{hc}} - (68.15 \pm 20.39)$  indicating a very steep dependence of  $\tau_{\text{cor}}$  on  $\Gamma_{\text{hc}}$ . Although, it can be seen that individual sources do not necessarily follow a positive trend, the overall tendency of our sample dictates that steepening of  $\Gamma_{\text{hc}}$  is associated with higher  $\tau_{\text{cor}}$ . The observed correlation between  $\tau_{\text{cor}}$  and  $\Gamma_{\text{hc}}$  could be explained by the fact that harder X-rays from hot corona illuminating the warm corona above a cold disk can give rise to radiative or thermally driven outflow from the outer warm corona layer which reduces its optical depth. The above proposed explanation has to be justified by multi-wavelength variability studies.

Further, we explored the distribution of r-value between  $\log q_{\text{h}}$  and  $\Gamma_{\text{hc}}$ . Considering the scatter of points, we obtained a Pearson’s r-value centered at  $-0.37 \pm 0.08$  at  $\gg 99\%$  confidence level (see Appendix B for details). The slope of best fit line (shown as grey dashed line Fig. 6 (a)) is again quite high,  $\log q_{\text{h}} = (-1.20 \pm 0.40) \Gamma_{\text{hc}} - (20.09 \pm 0.73)$ . On close inspection we notice that one observation corresponding to ESO198-G24 (red diamonds), one observation of PG0844+349 (magenta diamonds), RE1034+396 (cyan solid circles) and one observation of UGC 3973 (cyan diamonds) broadly contribute to large dispersion in these figures. They are also explicitly annotated in Fig. 6. PG0844+349 is a case of high line of sight absorption ( $\gtrsim 10^{22}$



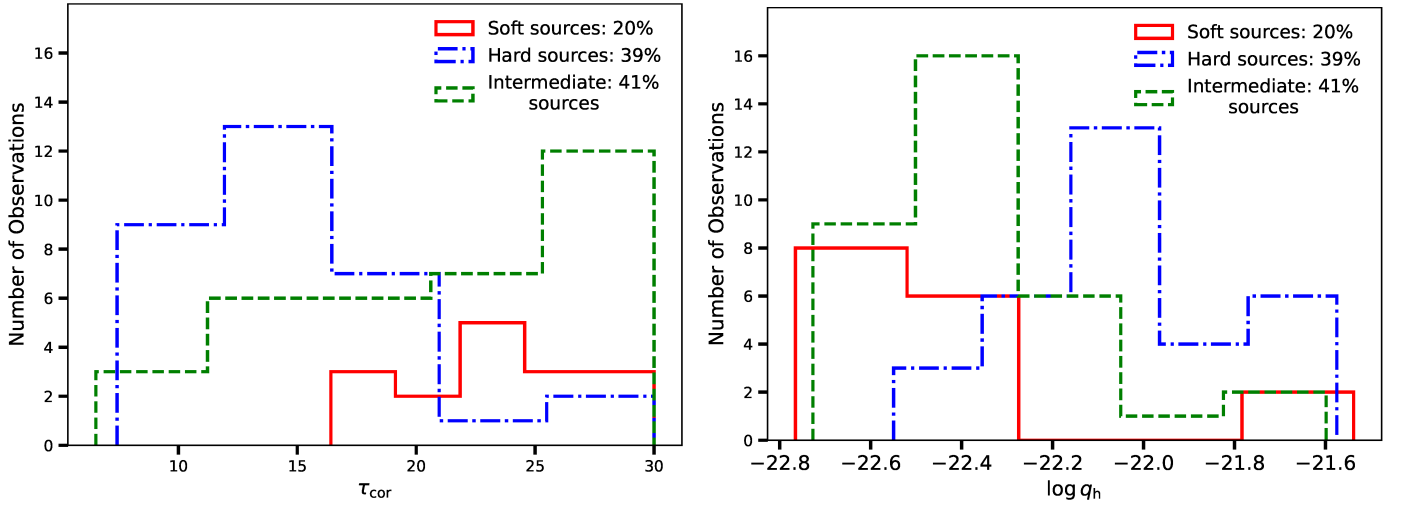


Fig. 5: Distribution of the warm corona optical depth,  $\tau_{\text{cor}}$  (left), and internal heating,  $\log q_h$  (right), from fitting the total model described in Sect. 4. Blue histogram denotes sources with  $\Gamma_{\text{hc}} \leq 1.7$ , red –  $\Gamma_{\text{hc}} \geq 2$  (soft) and the rest are denoted by green. The percentages denote fraction of total sample consisting of soft, hard or intermediate type sources.

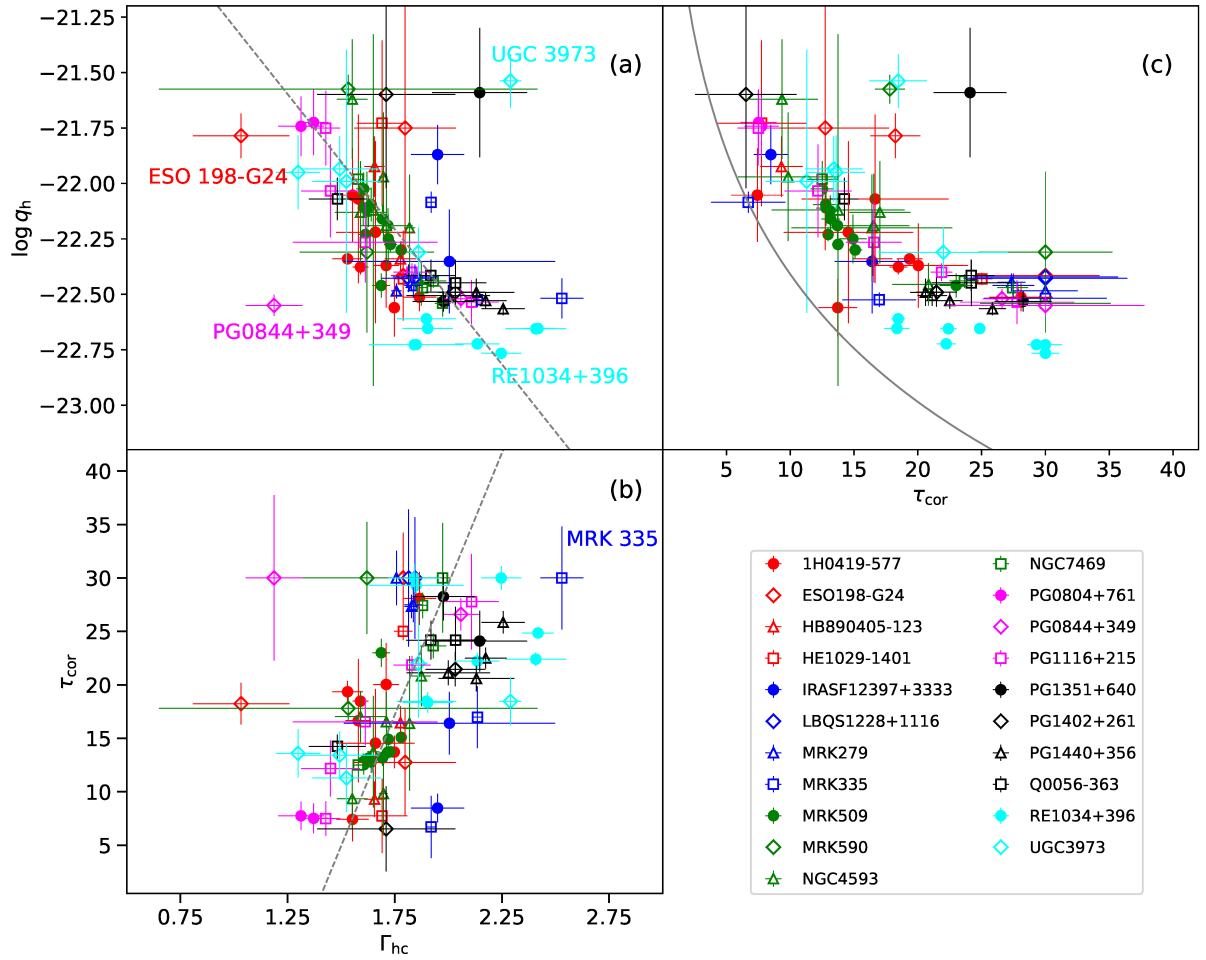


Fig. 6: Scatter plots showing the relationship between internal heating ( $\log q_h$ ) inside warm corona with hot corona spectral index  $\Gamma_{\text{hc}}$  (a), optical depth ( $\tau_{\text{cor}}$ ) of warm corona with  $\Gamma_{\text{hc}}$  (b) and variation of  $\log q_h$  vs  $\tau_{\text{cor}}$  (c). The best fit linear regression is indicated by grey dashed line. The grey solid curve in top-right panel corresponds to  $\chi = 1$  (Eq. 4), marking the boundary between active  $\chi < 1$ , and passive disk with  $\chi > 1$ . Different symbols associated with sources are given in bottom right.

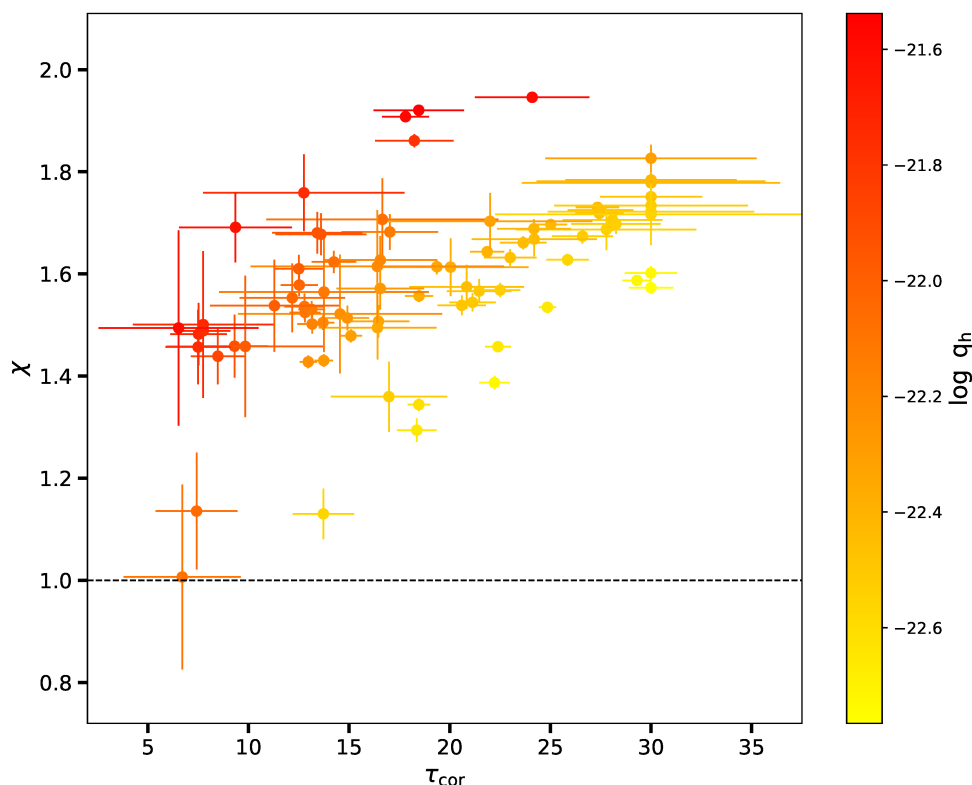


Fig. 7: Scatter plot showing the dissipation factor  $\chi$  against warm corona optical depth  $\tau_{\text{cor}}$  color coded by total internal heating value shown on the side color bar. Black dotted line at  $\chi=1.0$  denotes the transition region between passive disk –  $\chi>1$ , and active disk –  $\chi<1$ .

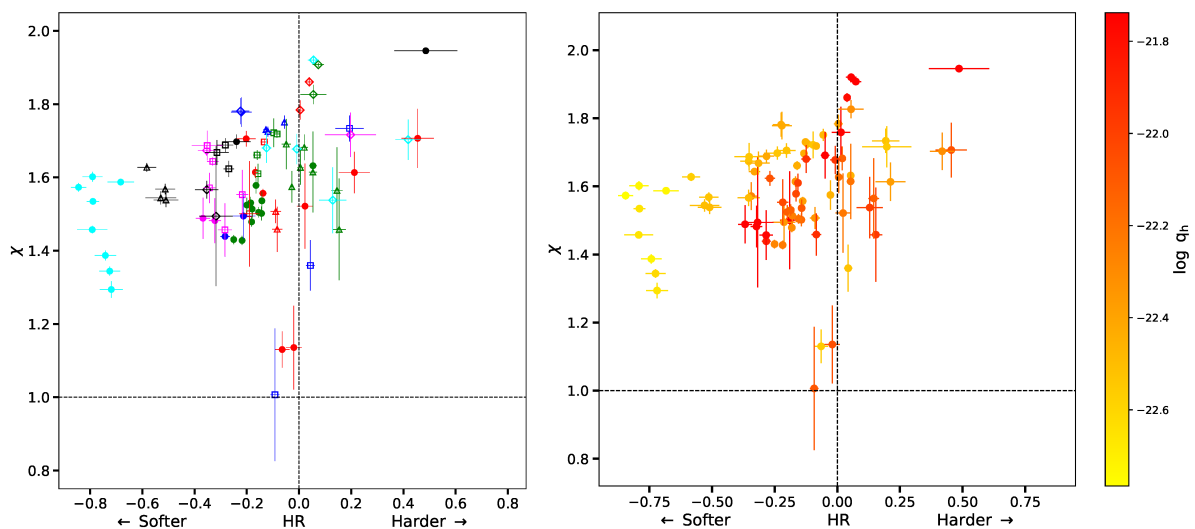


Fig. 8: Plots showing hardness ratio versus dissipation factor divided into four quadrants with dashed lines given by  $\text{HR}=0$  and  $\chi = 1$ , the latter being a transition between passive and active disk. Different symbols associated with sources are the same as in Fig. 6.

$\text{cm}^2$ ) which is not adequately modeled using our simplistic warm absorber model. UGC 3973 is a prototypical source with almost negligible reflection component (Gallo et al. 2011). This is also observed from our analysis where the soft-excess strength of this source is one of the highest, dominating the entire spectrum. The one particular observation (ObsID:400070301) contributing to deviation has a large soft excess strength and also an extremely high dissipation factor which could be the cause of dispersion in our scatter diagram. Similar explanation is possible behind

the dispersion seen in one particular observation of ESO 198-G24 (ObsID: 305370101) with large soft excess strength of  $\sim 14$ , which is largest in the entire sample. RE1034+396 is again a prototypical source with persistently large soft excess emission at Eddington fraction greater than one. As argued by Kaufman et al. (2017), the contribution to soft-excess emission at such super-Eddington accretion rates could be due to dominance of bulk Comptonization occurring due to turbulence in disk atmosphere. Nevertheless, higher warm corona heating corresponds

to the harder hot corona emission, which may suggest a common mechanism responsible for heating of both coronae.

Judging by the variation between optical depth with total internal heating (Fig. 6 (c)), there is an inverse non-linear relation between these two parameters. The grey solid line in top right panel represents the boundary between passive disk with  $\chi > 1$  and active disk with  $\chi < 1$  and two observations (corresponding to 1H0419-577 and Mrk 335) are located very close the boundary. PG1402+216 is also close to the boundary if considering error bars. These may indicate the possibility of transition between the above two configurations. While, most observations are well within the dissipative warm corona regime on top of a passive disk, we notice as the optical depth decreases, the data points approach the  $\chi=1$  line.

The dependence of dissipation rate  $\chi$  on warm corona optical depth and total internal heating is shown in Fig. 7. Extremely high values of  $\chi$  were observed in few cases of sources having large  $\tau_{\text{cor}}$  and  $\log q_{\text{h}}$ . On the other hand, a number of points lie below  $\chi = 1.2$ . These usually have  $\tau_{\text{cor}} < 20$  and  $\log q_{\text{h}} > -22.4$ . Comparing with Fig. 5 (right) and Fig. 6 (b), these belong to a small sub-sample of observations falling under the intermediate range of  $\Gamma_{\text{hc}}$  values of 1.7–2.0, which suggest a less active warm corona. Hence, the standard accretion disk is actively producing seed photons which can lead to efficient cooling of hot corona as well, leading to overall softening of photon index. Nonetheless, majority of points are confined to  $\chi$  values between 1.2–1.7 which is in accordance with computations performed by Petrucci et al. (2020, see Fig.2) and earlier estimates of warm corona properties (P18), requiring large amount of energy dissipation inside warm corona to reproduce the soft-excess.

Next, we compare the fraction of energy dissipated inside the warm corona against the HR, calculated using Eq. 8. As shown in Fig. 8 (left), observations populate the top two quadrants almost equally, with few points close to the  $\chi=1$  line. By looking at the points restricted to the given source, we see that the amount of energy dissipated in warm corona depends on the epoch of observation without large change in HR. It suggests that even though rate of dissipation changes inside the warm corona, the relative emission from hot and warm corona is unaffected. It may be possible that a common source of mechanical heating for both coronae can influence them in such a way as to strike a balance between their emission and maintain similar HRs.

Similar distribution of  $\chi$  versus HR, now color-coded by the total internal heating of warm corona is shown in Fig. 8 (right), where we see that the points corresponding to high values of heating seem to be restricted close to  $\text{HR} \approx 0$ . Those cases are also associated with lower values of warm corona optical depth and low/hard values of  $\Gamma_{\text{hc}}$  as evident in Figs. 6 and 7, respectively. While the HR values are not indicative of  $\Gamma_{\text{hc}}$ , it does suggest that comparable emission from both hot and warm corona could actually be heavily influenced by stronger heating.

Such a dominance of hot corona could indicate onset of some strong outburst from the inner region of the disk. As shown by K rding et al. (2006), quasars with high radio loudness occupy the hard state and hard-intermediate state in the disk fraction luminosity diagrams (DFLDs). However, a direct comparison of Fig. 8 with DFLD is not possible since we do not take into account the energetics of an accretion disk, but the coincidence of high heating values associated with ‘HR  $\approx 0$ ’ state is quite striking feature. Due to HR being slightly biased towards soft X-ray energies (as discussed in the beginning of Sect. 5.2), possibly observations close to zero value of HR actually correspond to harder states (HR  $> 0$ ). As seen from the figure, those states correspond to high internal heat dissipation inside the warm corona. Strong

outflows launched from disk can also be the cause of destruction of warm corona, explaining the smaller values of optical depth.

### 5.3. Warm corona in different AGN

For our further analysis, we adopted black hole masses and accretion rates from P18 and Bianchi et al. (2009, and references therein). For almost all sources the black hole mass has been estimated and is given in the last column of Table 1. Also the Eddington luminosity to bolometric luminosity ratio that directly corresponds to the accretion rate has been evaluated, and we list this quantity in the third column of Table 3.

The Fig. 9 displays warm corona properties as a function of accretion rate and black hole mass, the latter represented by color bar. The overall conclusion is that properties of the warm corona does not depend on accretion rate, where  $\chi$  and  $\tau_{\text{cor}}$  stay on the same level across wide range of Eddington ratios. We observe almost vertical dependence of  $\chi$  and  $\tau_{\text{cor}}$  for the sources at the same black hole mass. Only minute change may be noticed, when looking at the source of a given accretion rate. It may be caused by thermal instability recently predicted by Gronkiewicz et al. (2023). The dissipation fraction  $\chi$  displays a mild variation, decreasing from  $\sim 1.95$  to 1.40 with increasing accretion rate. Due to the coupled behavior of the standard disk with the warm and the hot coronae, to fully capture evolution of warm corona in AGNs, it is necessary to have multi-wavelength data across epochs where the AGN might have undergone large changes in accretion rate or total flux.

A noticeable decrease of the hardness ratio with increasing accretion rate is observed at right upper panel, indicating that emission from the warm corona, becomes stronger relative to the hot corona emission. This is also observed in the increase in SE with accretion rate (bottom right plot of Fig. 9). Hence, for highly accreting sources, the low value of hardness ratio is accompanied by the higher value of soft-excess strength. By studying these trends with larger data available in the future, it may indicate the importance of the warm corona in bright sources and the connection of warm corona dissipation rate with the accretion process.

### 5.4. Extent of the warm corona

As derived in Sect. 2.2, the normalization of TITAN/NOAR model,  $N_{\text{SE}}$ , can be related to the size of the warm corona, according to Eq. 6. Here, the extent of warm corona refers to the outer radius of warm corona. We estimated the radii for 19 sources with available distance measurement, totalling to 78 observations. Resulting radius from warm corona normalization, together with the distances to the source, are shown in Table 4. Only few sources– IRAS12397+3333, MRK 335, MRK 509, MRK 590, NGC 4593, NGC 7469, PG0844+349 and UGC 3973 have redshift independent distances measured by AGN dust reverberation mapping technique. For the remaining sources, we used the Hubble distance taken from NED (NASA/IPAC Extragalactic Database), with a Hubble constant  $H_0=68.7 \text{ km s}^{-1} \text{ Mpc}^{-1}$ .

The dependence of warm corona parameters, like optical depth, internal heating, dissipation fraction and soft excess strength, together with observed hardness ratio, on the warm corona radius is shown in Fig. 10. The extent of warm corona ranges between  $\sim 6.6$  to  $408 R_g$ , in accord with recent work by Kubota & Done (2018); Zoghbi & Miller (2023); Porquet et al. (2024); Vaia et al. (2024). The large values may be slightly overestimated due to negligence of spin of black hole (Porquet et al.

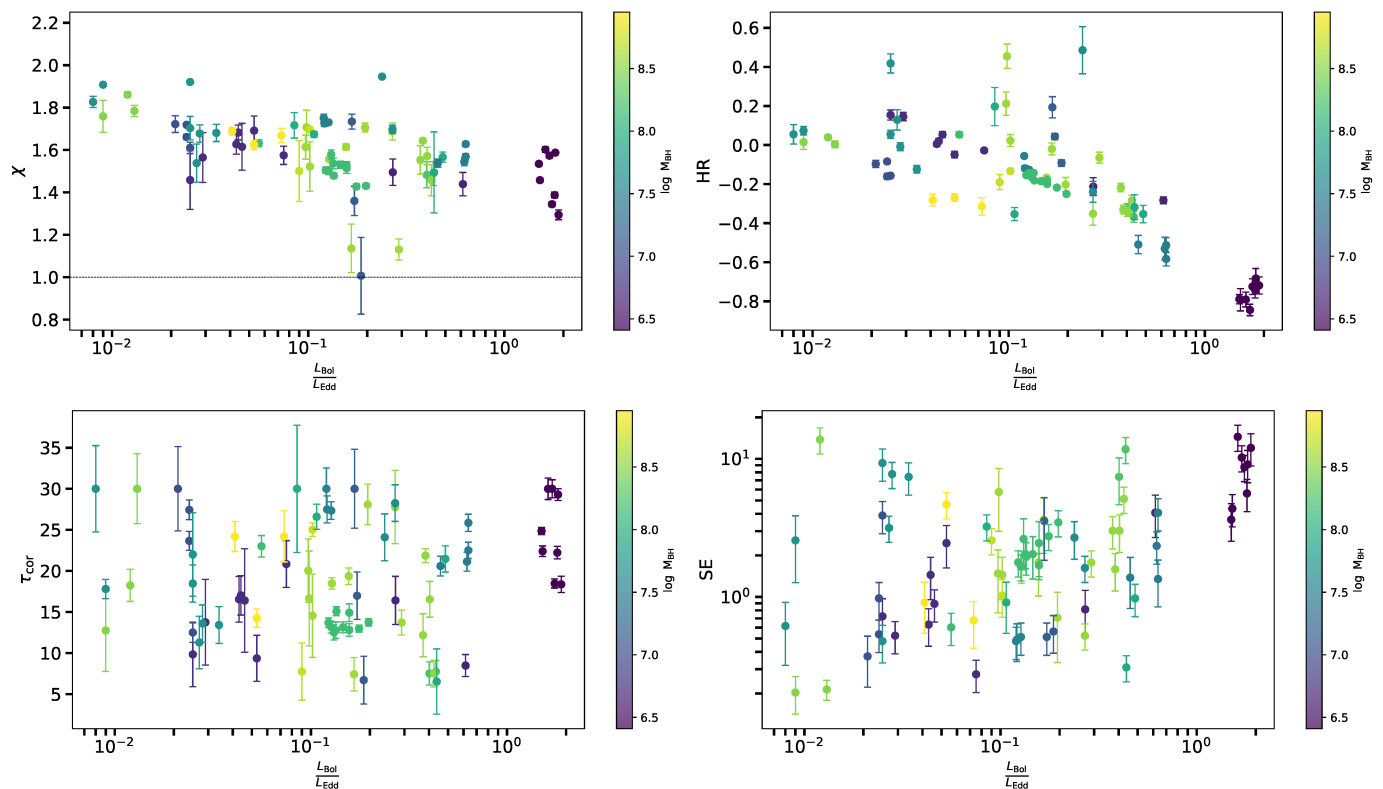


Fig. 9: Dependence of warm corona parameters on accretion rate taken from P18 - left panel, and soft excess strength and hardness ratio - right panel. The color map represents black hole mass of various AGN. Two sources-HB890405-123 and LBQS1228+1116 are not included in these figures due to unavailability of measurement of black hole mass.

2024), however  $R_{\text{cor}}$  values up to  $10^2 R_g$  have been recently reported by (Porquet et al. 2024) where they used the reXcor and RELAGN (Hagen & Done 2023) model.

The black hole masses in our sample spans across two order of magnitudes and the inner accretion flow may be at different evolutionary stages, as understood from hardness ratio plots presented in this paper. This adds a good amount of spread in the radius estimates and any tight correlation is difficult to obtain. Furthermore, the distance measurements are met with systematics of their own or dependence on the agreed upon  $H_0$  value. Nevertheless, we observe certain interesting trends in the data that point towards a transformation of warm corona layer with changing disk-corona geometry.

The first trend is shown in the top-most left panel of Fig. 10, where the  $\chi$  decreases as the warm corona expands, with black dotted line separating passive disk from active disk. Similarly, on the top-most right panel, we observe that spectra becomes increasing softer with expanding warm corona. This may suggest a growing importance of soft-excess emission with increasing size of warm corona. The cyan solid circles corresponding to RE1034+396 and red solid circles corresponding to 1H0419-577 add considerably to the dispersion. 1H0419-577 has complex absorption which could lead to hardening of spectra leading to large HR values. On the other hand, RE1034+396 is a super-Eddington accretor wherein, other physical processes might participate in soft-excess production as discussed in Kaufman et al. (2017). Overall, comparing this trend to the variation of  $\Gamma_{\text{hc}}$  in bottom right panel, we notice that it is independent of warm corona radius. Similarly,  $\tau_{\text{cor}}$  seems to be independent of the size of warm corona as well. This points towards the fact that while extrinsic property of warm corona (such as size) drives the magnitude of

soft-excess emission relative to hard X-rays, the intrinsic properties of warm corona (such as  $\tau_{\text{cor}}$ ) are possibly coupled to variation of hot corona, as already demonstrated in Fig. 6. For instance, as in middle left panel, we observe that  $\tau_{\text{cor}}$  does not show any coherent variation with warm corona radius. The soft excess strength SE seems to loosely depend on the radius, and increasing as the warm corona spreads over the disk. This conclusion is weakened due to presence of large scatter which could be a result of SE depending on both the intrinsic and extrinsic properties of warm corona.

At the bottom left panel of Fig. 10, we present the connection of accretion rate with the warm corona radius. An increase in  $L_{\text{Bol}}/L_{\text{Edd}}$  is accompanied by the increase in warm corona radius, which again on close inspection, is obeyed by individual sources. This result is particularly interesting since the accretion rates were determined using distinct method. It is well known that large changes in accretion rate are associated with changing inner disk structure. Comparing our observations of sources with accretion rate between 20–30 % of Eddington luminosity in Fig. 10, the warm corona radii is  $\sim 10^2 R_g$ . As demonstrated in Petrucci et al. (2013), this is consistent with inner disk radius between 6–10  $R_g$  which constitutes the hot corona. For Mrk 509, they showed that in such a scenario, both the hot and warm corona shared similar amount of accretion power and total luminosity. Thus, for accretion rates roughly below 10% of Eddington, we expect an onset of changes in coronal geometry as warm corona radius decreases, leading to unequal redistribution of energies between the two coronae. Mrk 1018 underwent a large drop in mass accretion rate from 8% to 0.6% which was accompanied by 60% drop in the soft-excess emission (Noda & Done 2018), Mrk 841 also displayed a diminishing UV/optical continuum,

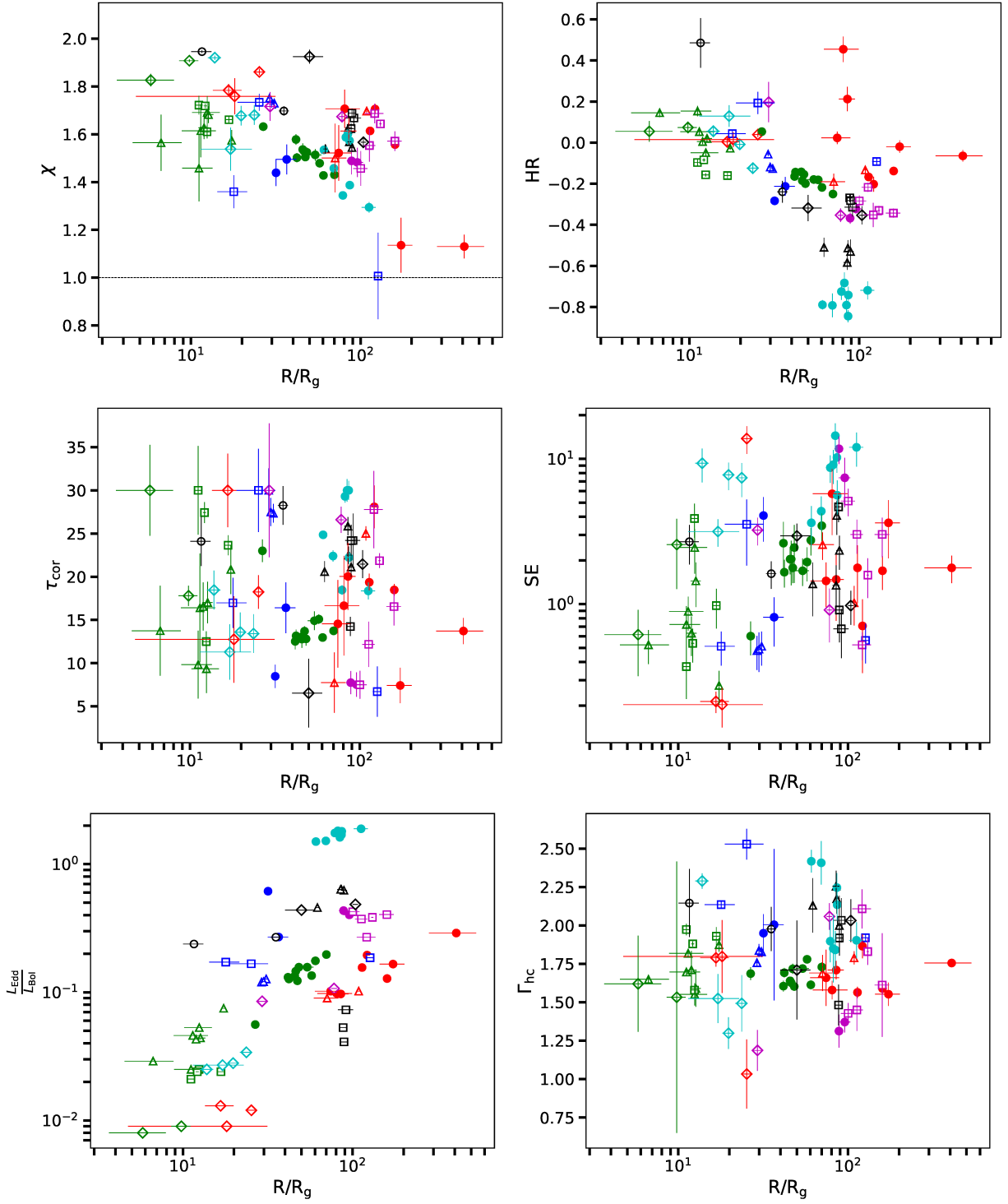


Fig. 10: Scatter plots showing the dependence of various warm corona properties and global parameters on the radius of warm corona, given in the units of gravitational radius. There are a total 20 sources consisting of 90 sources, out of which 8 sources have redshift independent distance measurement while for the remaining 12, Hubble distance was used. See text for details. Unique markers indicate different sources, same as Fig. 6.

associated with vanishing soft-excess (Mehdipour et al. 2023) and similar conclusions were drawn for Mrk 590 as well (Denney et al. 2014). Our results demonstrate that such variation may be associated with the evolution of the warm corona which may depend on the global accretion rate and its intrinsic properties in a complicated way. To capture the trigger of such evolution may be important in the context of changing ‘state’ AGNs, which show

correlated changes in Optical/UV continuum with accretion rate (Ricci & Trakhtenbrot 2023; Veronese et al. 2023, and references within).



Table 4: Estimates of warm corona radius  $R_{\text{cor}}$  from TITAN/NOAR normalization  $N_{\text{SE}}$  (Eq. 6), in terms of gravitational radii, for sources of known distances ( $D$ ).

Source $D$	ObsID	$N_{\text{SE}} = S/D^2$ [ $\times 10^{-7}$ ]	$R_{\text{cor}}$ [ $R_g$ ]	Source $D$	ObsID	$N_{\text{SE}} = S/D^2$ [ $\times 10^{-7}$ ]	$R_{\text{cor}}$ [ $R_g$ ]	
1H0419-577 459.83 Mpc	112600401	2.20±0.17	121.76 ± 4.58	NGC 7469 57.30 Mpc	112170101	1.77 ± 0.18	11.14 ± 0.57	
	148000201	0.97±0.45	80.62 ± 18.58		112170301	3.99 ± 0.31	16.75 ± 0.65	
	148000301	1.08±0.23	85.26 ± 9.24		207090101	2.20 ± 0.16	12.45 ± 0.46	
	148000401	24.80±15.0	408.55 ± 126.03		207090201	2.10 ± 0.08	12.15 ± 0.24	
	148000501	4.46±1.48	173.26 ± 28.75		PG0804+761	605110101	1.47 ± 0.23	95.72 ± 7.60
	148000601	0.82±0.32	74.28 ± 14.34		442.45 Mpc	605110201	1.26 ± 0.15	88.49 ± 5.27
ESO198-G24 200.89 Mpc	604720301	1.92±0.09	113.77 ± 2.79	PG0844+349	103660201	1.25 ± 0.10	77.75 ± 2.99	
	604720401	3.79±0.34	159.71 ± 7.10	390.00 Mpc	554710101	0.18 ± 0.02	29.29 ± 1.98	
	067190101	0.22 ± 0.08	16.67 ± 3.18	201940101	0.88 ± 0.02	130.86 ± 1.73		
HE1029-1401 384.82 Mpc	112910101	0.26 ± 0.38	18.12 ± 13.37	PG1116+215	201940201	0.76 ± 0.19	121.17 ± 15.20	
	305370101	0.50 ± 0.05	25.31 ± 1.35	554380101	1.30 ± 0.25	159.22 ± 15.48		
	110950101	1.06± 0.35	70.79 ± 11.71	781.54 Mpc	554380201	0.66 ± 0.11	112.85 ± 9.35	
IRAS F12397+3333 155.0 Mpc	203770101	2.51 ± 0.06	108.68 ± 1.28	554380301	0.52 ± 0.10	100.25 ± 9.54		
	202180201	1.32±0.12	31.75 ± 1.47	PG1351+640	205390301	0.26 ± 0.03	35.30 ± 2.41	
MRK 279 135.49 Mpc	202180301	1.76±0.49	36.68 ± 5.07	391.23 Mpc	556230201	0.03 ± 0.01	11.62 ± 1.58	
	302480401	1.64±0.08	30.96 ± 0.77	PG1402+261	400200101	0.64 ± 0.05	103.89 ± 3.76	
	302480501	1.45 ± 0.06	29.06 ± 0.58	728.43 Mpc	400200201	0.15 ± 0.06	49.99 ± 10.02	
MRK 335 85.90 Mpc	302480601	1.53 ± 0.11	29.90 ± 1.04	5010101	1.87 ± 0.09	85.87 ± 2.00		
	510010701	2.72 ± 1.39	25.28 ± 6.46	PG1440+356	5010201	2.01 ± 0.17	88.96 ± 3.69	
	600540501	68.5 ± 8.01	126.84 ± 7.42	351.87 Mpc	5010301	0.98 ± 0.05	62.04 ± 1.70	
	600540601	1.36 ± 0.55	17.88 ± 3.59	107660201	1.84 ± 0.17	85.10 ± 3.94		
Mrk 509 105 Mpc	0130720101	6.92±0.52	26.69 ± 0.46	Q0056-363 722.24 Mpc	102040701	0.50 ± 0.10	91.38 ± 9.25	
	0601390201	5.06±0.42	42.15 ± 1.76	205680101	0.47 ± 0.03	87.98 ± 3.22		
	0601390301	6.36±0.56	47.26 ± 2.10	401930101	0.48 ± 0.04	88.99 ± 4.06		
	0601390401	6.63±0.51	48.24 ± 1.85	RE1034+396	109070101	4.03 ± 0.22	69.57 ± 1.90	
	0601390501	5.01±0.16	60.41 ± 3.51	506440101	3.08 ± 0.09	60.8 ± 0.91		
	0601390601	14.02±0.85	70.09 ± 2.12	561580201	6.17 ± 0.33	86.05 ± 2.31		
	0601390701	8.31±1.45	54.03 ± 4.73	655310101	6.21 ± 0.33	86.36 ± 2.06		
	0601390801	6.09±0.51	46.25 ± 1.95	655310201	5.15 ± 0.18	78.62 ± 1.40		
	0601390901	4.93±0.21	41.63 ± 0.91	675440101	10.5 ± 1.99	112.25 ± 10.64		
	06013901001	9.38±0.72	57.38 ± 2.21	675440201	5.59 ± 0.26	81.87 ± 1.93		
	06013901101	5.92±0.42	45.60 ± 1.95	675440301	5.91 ± 0.16	84.20 ± 1.16		
MRK 590 87.10 Mpc	109130301	0.14 ± 0.10	5.79 ± 2.13					
	201020201	0.40 ± 0.10	9.79 ± 1.26					
NGC 4593 61.00 Mpc	059830101	2.55 ± 0.14	17.38 ± 0.41	UGC393	103862101	1.14 ± 0.76	17.12 ± 5.69	
	109970101	1.31 ± 0.49	12.48 ± 2.31	90.00 Mpc	400070201	2.17 ± 0.36	23.64 ± 1.96	
	740920201	1.10 ± 0.50	11.43 ± 2.31	400070301	0.74 ± 0.13	13.82 ± 1.25		
	740920301	1.05 ± 0.43	11.15 ± 2.27	400070401	1.52 ± 0.24	19.77 ± 1.55		
	740920401	0.38 ± 0.24	6.67 ± 2.13	502091001	1.00 ± 0.15	16.06 ± 1.22		
	740920501	1.36 ± 0.19	12.69 ± 0.87					
	740920601	1.20 ± 0.17	11.94 ± 0.86					

**Notes:**

Two sources- HB890405-123 and LBQS1228+1116 are not included here due to un-availability of black hole mass measurements. Details on distance measurement ( $D$ ) is given in Sect. 5.4.

## 6. Discussion

### 6.1. Nature of the warm corona

We have obtained an optically thick warm corona with mean value of  $\tau_{\text{cor}} = 18.26 \pm 0.12$ , which agrees with vast majority of optical depth values previously reported (Petrucci et al. 2018; Jiang et al. 2019b; Middei et al. 2019b, and references therein). Our results also indicate the requirement of relatively high internal heating of the warm corona, which shows two peaks. The first peak

corresponds to sources with hard photon index for which  $\log q_{\text{h}} = -22.0$ , and the second to sources with soft and intermediate range of  $\Gamma_{\text{hc}}$  for which  $\log q_{\text{h}} = -22.5$ . The mean internal heating for all observations results in  $q_{\text{h}} = 5.62 (\pm 0.38) \times 10^{-23} \text{ erg s}^{-1} \text{ cm}^{-3}$ . Both results confirm the earlier expectation that the warm corona which is cooled by Compton process has to be internally heated to stay in balance with an accretion disk (Róžańska et al. 2015).

Recently, more realistic treatment of magnetically heated disk/corona atmosphere confirmed the existence of warm corona

with optical depth up to 50 (Gronkiewicz et al. 2023). The value of the mean internal heating reported in this work belongs to moderately high level of dissipation when compared to the parameter space considered by Gronkiewicz et al. (2023). Furthermore, the range of  $\log q_h$  resulting from our fitting procedure is prone to classical thermal instability, a key aspect of magnetically supported disks (MSDs) with dominance of Comptonization and free-free emission, forming the warm corona.

All the 82 observations, corresponding to 21 sources, point towards the existence of dissipative warm corona on top of cold, accretion disk. The emergent soft-excess emission spectra is smooth, as is expected in a Compton dominated warm layer with dissipation fraction ranging from 1 to 1.95. This is aligned with the claims of copious amounts of energy dissipation in the warm layer suggested by radiative transfer models (Ballantyne & Xiang 2020; Xiang et al. 2022; Kawanaka & Mineshige 2024) and as well as magneto-hydrodynamic simulations (Hirose et al. 2006; Jiang et al. 2019b; Mishra et al. 2020) which could lead to the origin of such a warm layer.

We noticed mild correlations of warm corona parameters with the photon index of hot corona being modeled by the independent NTHCOMP model. It must be noted that we do not impose any a priori link between the parameters of the two Comptonizing coronae. All trends between model parameters are the result of their adjustment to the observed spectral shape. Our analysis indicated that hard sources (with lower value of  $\Gamma_{hc}$ ) are associated with warm corona having lower optical depth and higher internal heating. Conversely, softer sources indicate warm corona of higher optical depth and lower heating. It may be possible that at larger optical depths, the warm corona is acting as the source of extra seed photons entering the hot corona, and cooling this region faster which results in softening the  $\Gamma_{hc}$  index. Such an instance was recently reported in case of Mrk 359 (Middei et al. 2020), where observed spectral variability detected by *XMM-Newton* and *NuSTAR* mission was interpreted by two-corona model, in which the outer disk is covered by warm corona, and the warm corona's photons may cool the hot corona through Comptonization. On the other hand, a flat  $\Gamma_{hc}$ , indicating an extremely hard hot corona, can lead to destruction of warm corona by depriving it of seed photons and causing extreme heating.

The above ideas are model dependent and subject to limitations for two reasons. Firstly, we set strict constraints on the  $\Gamma_{hc}$  by freezing the temperature of the hot corona (Table 2). Secondly, we assumed in all TITAN/NOAR models the same photon index of 1.80 of the hard external illumination from the hot corona. While this is standard assumption for majority of AGNs (Ricci et al. 2017; Akylas & Georgantopoulos 2021), it can affect the inferred warm corona properties, especially for AGNs with very steep and very flat  $\Gamma_{hc}$ . Nevertheless, Petrucci et al. (2013) demonstrated that hot corona illumination is a factor of 2 lower than total warm corona luminosity, therefore, it has less effect on warm corona properties than internal mechanical heating. In addition, Xiang et al. (2022), with the use of the reXroc model, have shown that photon index of external illumination has negligible effect on the emitted soft X-ray spectrum. This was the case even for low coronal height in their lamp-post model.

In the framework of our model, we do not observe the transition from the state of active warm corona and passive disk to the state where disk becomes dissipative. (Gronkiewicz et al. 2023) demonstrated that classical thermal instability occurs at the base of the warm corona, and can trigger changes of disk/corona radiative equilibrium, leading to the build-up of the warm optically thick plasma above an accretion disk on the timescales of the

order of days. Deeper multi-epoch data in different energy bands are needed to fully test this scenario.

One question still remains to be answered, that is, what is the origin of this heating inside the warm corona? The coincidence of heating values within the realm of MSDs can give some hints that magnetic fields are responsible for heating upper layers of disk atmosphere (Hirose et al. 2006; Begelman et al. 2015; Gronkiewicz et al. 2023). Multi-dimensional MHD simulations made by different groups (Turner et al. 2003; Beckwith et al. 2009; Takeuchi et al. 2010; Mishra et al. 2020; Wielgus et al. 2022; Liska et al. 2022) have shown the requirement of strong magnetic fields at large scale height of stable accretion disks, is consistent with large optical depths  $\gg 5$  of the warm plasma, observed in our sample.

## 6.2. Comparison with reXcor model

Recently, a similar model on the soft-excess emission (i.e., reXcor; (Ballantyne 2020; Xiang et al. 2022)) was tested on a smaller subset of sources from the same sample as in our work (Ballantyne et al. (2024), hereafter B24). The origin of the heating of the warm corona in this model is connected to purely viscous dissipation of accretion energy by standard disk, and the total dissipated energy is divided between three emitting regions: cold disk, warm corona and hot corona. Given that, a hot corona needs to be powered as well, the authors concluded that 50% of the total accretion energy powers the warm corona, which supports the existence of large level of heating. Since, we do not restrict  $\log q_h$  to any particular physical mechanism, it provides an upper limit to realistic level of heating that can exist in the warm corona. It would be interesting to explore heating levels for sources which possess active disks, and we plan to do it in our future research.

Our implementation of composite X-ray spectral model differs from B24 in two respects. While they approximated the hard X-ray tail of spectra with a powerlaw, we used more physical NTHCOMP model, self-consistently connecting the seed photon temperature of 7 eV. However, the main difference arises in the soft X-ray emission band where, we employ the TITAN/NOAR model, as oppose to reXcor by B24. Overall, our total model has 3 d.o.f less than B24.

As a result of spectral fitting, B24 reached the same conclusion that the warm corona has to be highly dissipative, which indicates the dominance of external agents such as magnetic field playing an important role in maintaining a warm corona. The authors concluded the presence of  $\sim 50-70\%$  heating fraction thus supporting the production of soft-excess from warm corona. They obtained a mean optical depth of 14, which is close to our estimates. However, there is a considerable difference in the relation between optical depth and internal heating of the warm corona. B24 found higher amount of heating fraction in warm corona for larger optical depth which is in opposition to our results. This may be an artifact of different model construction.

Next, B24 obtained a 'v' shaped trend between both warm corona optical depth and heating fraction with accretion rate. We did not observe any particular trend between the same parameters from our study. This could be attested to the fact that our model is essentially independent of an accretion rate. Infact, the total warm corona emission is mainly a resultant of reprocessed emission of the illuminated radiation originating in the hot corona as well as from the cold disk, and dissipative emission from inside the warm corona. From our studies, we merely observe an overall effect of how these micro-processes vary with global accretion rate which was estimated using distinct method in P18. So, the

overall differences in setup of the two models as described above and in Sect. 2 lead to such trends. Nevertheless, they observed an increase in warm corona flux with observed accretion rates, which could be due to increasing radial size of warm corona. We have drawn the same conclusion after estimating the size of warm corona and studying how it depends on an accretion rates, thus strengthening the overall goals of both methods.

While the *reXcor* model considers deposition of fraction of accretion energy in the form of reflection from lamppost like corona, its effect is not very significant in determining the shape of soft-excess (Ballantyne & Xiang 2020). Application of *reXcor* model to observations of a sample of Seyfert 1 galaxies revealed a low fraction of the total accretion energy budget contributing towards reflection (B24, Porquet et al. 2024), when compared to the amount of heating. Additionally, the lamppost geometry for hot corona is currently refuted by X-ray polarimetric measurements of few AGNs (Pal et al. 2023; Tagliacozzo et al. 2023) and X-ray binaries (Jana & Chang 2024). Another difference between our model with *reXcor* is that the later includes the dependence on black hole spin. At high ionization levels such as considered in the warm corona, the effect of relativistic blurring is negligible. This effect has also been shown by Xiang et al. (2022) using *reXcor*. Thus, our negligence of spin has less effect on the inferred properties of warm corona.

Despite differences in the design of two models, our global results are in agreement, that is, the requirement of extra heating inside warm corona to properly describe the smooth, soft-excess spectrum and increasing radial size of warm corona with accretion rate.

### 6.3. Warm corona with an accretion disk

We found that presence of warm corona in the inner regions of accretion disk can adequately describe the soft-excess feature in a variety of AGNs, spread across wide range of accretion rates and black hole masses (Fig. 9). One of the most interesting results of our work is the evolution of radial extent of warm corona with accretion rate (Fig. 10, bottom left). It must be noted that no link between comptonized emission and soft UV emission was imposed a priori. The model adjusts its parameters to fit the data. We observed that as the accretion rate of the system increases, the warm corona radius increases. But, similar trends were not observed between accretion rate and warm corona properties or between warm corona radius and its properties. We speculate that this apparent dis-connect could arise due to the standard disk playing a very different role from that of the hot corona in the formation and evolution of warm corona. Changes in the disk are more prone to driving the external properties of the warm layer such as its extent Fig. 10 (bottom left panel) or partial contribution to soft-excess emission Fig. 9 (bottom right panel). On the other hand, innate features like heating and optical depth are largely influenced by the hot corona (hence the overall inner disk geometry) as evident from trends shown in Fig. 6. Recent study by (Waddell et al. 2023, accepted for publication in A&A), suggested external factors like winds or magnetic fields influencing the properties of warm corona. This study conducted on 200 AGNs in the eROSITA Final Equatorial Depth Survey (eFEDs) revealed an increase in soft-excess emission with accretion rate. They associated a failed wind settling on the disk, forming the warm corona. In such a scenario, accretion rate will not directly influence warm corona optical depth or internal heating. It also depends at what location the winds settle since heating (as well as disk flux injecting into the warm corona) is not uniform throughout the radial extent of a disk.

In keeping with the prevailing idea of changing disk-corona system with accretion rate, at lower values of  $L_{\text{Bol}}/L_{\text{Edd}}$ , where the disk is thought to be truncated, we found that extension of warm corona is lowest. This indirectly indicates that the surface area of warm corona decreases as the disk recedes from the black hole, making the warm layer photon starved. At such low  $L_{\text{Bol}}/L_{\text{Edd}}$ , hot flow can occur close to the black hole (Yuan & Narayan 2014) and any warm corona that survives the absence of a cold disk, now begins to disappear as it competes for seed photons against the powerful hot corona. Strong magnetic field powering the hot corona could leak into the warm corona as well, confining it to smaller optical depths. On the other hand, at  $L_{\text{Bol}}/L_{\text{Edd}} > 0.1$ , we noticed the increase in warm corona surface area, due to appearance of the disk which replenishes the warm corona with seed photons for Compton cooling, hence stabilizing it in the process. This is also reflected in slightly higher values of soft-excess strength.

At intermediate values of an accretion rate, there is a wide spread in the scatter plot which could be due to changing state phenomena suggested to occur at  $L_{\text{Bol}}/L_{\text{Edd}} \sim 0.01-0.02$  (Noda et al. 2011; Mahmoud & Done 2020; Ricci & Trakhtenbrot 2023). B24 also observed an abrupt change in optical depth and heating fraction at accretion rates  $\approx 0.1-0.2$ , suggesting a changing state behavior. In our work, it is interesting to notice how individual sources still obey a positively increasing trend, being located at different regions of accretion rate–warm corona radius scatter space, hinting at variety of evolutionary stages for each sources. In summary, we found that expanse of warm corona layer is intricately linked to the standard accretion disk and less dependent on the hot corona. We show that even with a crude estimate, changing accretion states in AGNs affect the warm corona, hence the emission in the soft X-ray band. It will pave the way to test such models or relations on multi-epoch observations of singular sources, which are better equipped for understanding the changing complex inner-disk geometry.

## 7. Conclusions

In this work, we tested a model of dissipative warm corona on a sample of 21 AGNs with widely distributed redshifts, accretion rates and black hole masses. The final emission responsible for soft X-ray excess was obtained by radiative transfer computations with TITAN/NOAR code, where the internal heating was balanced by Compton cooling with all other radiative processes as photoionization and bremsstrahlung were taken into account, simultaneously. The final grid of models for wide range of parameters was used in spectroscopic analysis of the 0.3–10 keV EPIC-pn, allowing us to put constraints on optical depth of the warm corona and the value of internal heating. Then, we searched for correlated trends of warm corona properties with global parameters of AGN, such as accretion rate and hardness ratios. Finally, our model allowed us to estimate the extent of warm corona being in harmony with our assumed model of the inner disk geometry.

1. All observations point towards the existence of a dissipative warm corona with dissipation fraction in the range 1–1.95. Hence, most of the accretion energy is spent in the upper layers of warm corona. Changes in dissipation fraction are not accompanied by large change in hardness ratios which suggests a common origin of heating source for both hot and warm corona.
2. The average optical depth of warm corona in our sample is  $\sim 18.26 \pm 0.12$  and average internal heating  $\sim 5.62(\pm 0.38) \times$

$10^{-23}$  erg  $s^{-1}$   $cm^3$ . This region of parameter space is consistent with recent studies of the soft-excess in AGNs. The emergent soft X-ray spectra are smooth, as expected due to Compton smearing of emission/absorption lines.

3. The sources with low/hard hot corona photon index are associated with warm corona having lower optical depth but stronger internal heating.
4. While the soft-excess emission is common in sources spanning a wide range of accretion rates, the fundamental properties of the warm corona such as optical depth and internal heating do not exhibit any dependence on accretion rates.
5. Radial expanse of warm corona varies through a large range of values, starting as low as 6.6 to 408  $R_g$ . For each individual source as well as a whole, we found a positive trend with accretion rate, suggesting a connection between warm corona and standard accretion disk.

Future work will improve our warm corona emission model by stronger tying of parameters between different model components used to build the total fitting model. On the other side, combining deep broadband UV/Optical data with hard X-rays will give key insights into the disk-warm corona interplay.

*Acknowledgements.* This research was supported by the Polish National Science Center grants No. 2021/41/B/ST9/04110. BP would like to thank Alex Markowitz for riveting discussions on the spectral modeling of soft-excess. BP would also like to thank colleagues, Tathagata Saha and Parikshit Partha Biswas for helpful discussion on statistical & data analysis. S.B. is an overseas researcher under the Postdoctoral Fellowship of Japan Society for the Promotion of Science (JSPS), supported by JSPS KAKENHI Grant Number JP23F23773. StB acknowledges funding from PRIN MUR 2022 SEAWIND 2022Y2T94C, supported by European Union - Next Generation EU, and from INAF LG 2023 BLOSSOM.

## References

- Abrassart, A. & Dumont, A. M. 2001, in American Institute of Physics Conference Series, Vol. 599, X-ray Astronomy: Stellar Endpoints, AGN, and the Diffuse X-ray Background, ed. N. E. White, G. Malaguti, & G. G. C. Palumbo, 489–492
- Akritas, M. G. & Bershad, M. A. 1996, *ApJ*, 470, 706
- Akylas, A. & Georgantopoulos, I. 2021, *A&A*, 655, A60
- Arnaud, K. A. 1996, in Astronomical Society of the Pacific Conference Series, Vol. 101, Astronomical Data Analysis Software and Systems V, ed. G. H. Jacoby & J. Barnes, 17
- Ballantyne, D. R. 2020, *MNRAS*, 491, 3553
- Ballantyne, D. R., Sudhakar, V., Fairfax, D., et al. 2024, *MNRAS*, 530, 1603
- Ballantyne, D. R. & Xiang, X. 2020, *MNRAS*, 496, 4255
- Barret, D., Albuouys, V., Herder, J.-W. d., et al. 2023, *Experimental Astronomy*, 55, 373
- Beckwith, K., Hawley, J. F., & Krolik, J. H. 2009, *ApJ*, 707, 428
- Begelman, M. C., Armitage, P. J., & Reynolds, C. S. 2015, *ApJ*, 809, 118
- Behar, E., Peretz, U., Kriss, G. A., et al. 2017a, *A&A*, 601, A17
- Behar, E., Peretz, U., Kriss, G. A., et al. 2017b, *A&A*, 601, A17
- Bianchi, S., Guainazzi, M., & Chiaberge, M. 2006, *A&A*, 448, 499
- Bianchi, S., Guainazzi, M., Matt, G., Fonseca Bonilla, N., & Ponti, G. 2009, *A&A*, 495, 421
- Boissay, R., Ricci, C., & Paltani, S. 2016, *A&A*, 588, A70
- Cappi, M., De Marco, B., Ponti, G., et al. 2016a, *A&A*, 592, A27
- Cappi, M., De Marco, B., Ponti, G., et al. 2016b, *A&A*, 592, A27
- Chalise, S., Lohfink, A. M., Chauhan, J., et al. 2022, *MNRAS*, 517, 4788
- Chatzikos, M., Bianchi, S., Camilloni, F., et al. 2023, *Rev. Mexicana Astron. Astrofis.*, 59, 327
- Crummy, J., Fabian, A. C., Gallo, L., & Ross, R. R. 2006, *MNRAS*, 365, 1067
- Czerny, B., Nikolajuk, M., Różańska, A., et al. 2003, *A&A*, 412, 317
- Denney, K. D., De Rosa, G., Croxall, K., et al. 2014, *ApJ*, 796, 134
- Di Gesu, L., Costantini, E., Arav, N., et al. 2013, *A&A*, 556, A94
- Done, C., Davis, S. W., Jin, C., Blaes, O., & Ward, M. 2012, *MNRAS*, 420, 1848
- Dumont, A. M., Abrassart, A., & Collin, S. 2000, *A&A*, 357, 823
- Dumont, A.-M., Collin, S., Paletou, F., et al. 2003, *A&A*, 407, 13
- Dunn, R. J. H., Fender, R. P., Körding, E. G., Belloni, T., & Cabanac, C. 2010, *MNRAS*, 403, 61
- Ebrero, J., Costantini, E., Kaastra, J. S., et al. 2010, *A&A*, 520, A36
- Fabian, A. C., Miniutti, G., Gallo, L., et al. 2004, *MNRAS*, 353, 1071
- Gabriel, C., Denby, M., Fyfe, D. J., et al. 2004, in Astronomical Society of the Pacific Conference Series, Vol. 314, Astronomical Data Analysis Software and Systems (ADASS) XIII, ed. F. Ochsenbein, M. G. Allen, & D. Egret, 759
- Gallo, L. C., Miniutti, G., Miller, J. M., et al. 2011, *MNRAS*, 411, 607
- García, J., Dauser, T., Lohfink, A., et al. 2014, *ApJ*, 782, 76
- García, J., Dauser, T., Reynolds, C. S., et al. 2013, *ApJ*, 768, 146
- García, J. & Kallman, T. R. 2010, *ApJ*, 718, 695
- García, J. A., Kara, E., Walton, D., et al. 2019, *ApJ*, 871, 88
- Gierliński, M. & Done, C. 2004, *MNRAS*, 349, L7
- Gliozzi, M. & Williams, J. K. 2020, *MNRAS*, 491, 532
- Gordon, C. & Arnaud, K. 2021, PyXspec: Python interface to XSPEC spectral-fitting program, Astrophysics Source Code Library, record ascl:2101.014
- Gronkiewicz, D. & Różańska, A. 2020, *A&A*, 633, A35
- Gronkiewicz, D., Różańska, A., Petrucci, P.-O., & Belmont, R. 2023, *A&A*, 675, A198
- Guainazzi, M., Bianchi, S., & Dovčiak, M. 2006, *Astronomische Nachrichten*, 327, 1032
- Haardt, F. & Maraschi, L. 1993, *ApJ*, 413, 507
- Hagen, S. & Done, C. 2023, RELAGN: AGN SEDs with full GR ray tracing, Astrophysics Source Code Library, record ascl:2306.023
- Hirose, S., Krolik, J. H., & Stone, J. M. 2006, *ApJ*, 640, 901
- Jana, A. & Chang, H.-K. 2024, *MNRAS*, 527, 10837
- Janiuk, A., Czerny, B., & Madejski, G. M. 2001, *ApJ*, 557, 408
- Jiang, J., Walton, D. J., Fabian, A. C., & Parker, M. L. 2019a, *MNRAS*, 483, 2958
- Jiang, Y.-F., Blaes, O., Stone, J. M., & Davis, S. W. 2019b, *ApJ*, 885, 144
- Jin, C., Ward, M., Done, C., & Gelbord, J. 2012, *MNRAS*, 420, 1825
- Kaufman, J., Blaes, O. M., & Hirose, S. 2017, *MNRAS*, 467, 1734
- Kawanaka, N. & Mineshige, S. 2024, *PASJ*, 76, 306
- Körding, E. G., Jester, S., & Fender, R. 2006, *MNRAS*, 372, 1366
- Kubota, A. & Done, C. 2018, *MNRAS*, 480, 1247
- Kumari, K., Dewangan, G. C., Papadakis, I. E., et al. 2023, *MNRAS*, 521, 4109
- Liska, M. T. P., Musoke, G., Tchekhovskoy, E., Porth, O., & Beloborodov, A. M. 2022, *ApJ*, 935, L1
- Longinotti, A. L., Krongold, Y., Kriss, G. A., et al. 2013, *ApJ*, 766, 104
- Madaj, J. & Różańska, A. 2000, *A&A*, 363, 1055
- Magdziarz, P., Blaes, O. M., Zdziarski, A. A., Johnson, W. N., & Smith, D. A. 1998, *MNRAS*, 301, 179
- Mahmoud, R. D. & Done, C. 2020, *MNRAS*, 491, 5126
- Mason, K. O., Breeveld, A., Much, R., et al. 2001, *A&A*, 365, L36
- Matt, G., Marinucci, A., Guainazzi, M., et al. 2014, *MNRAS*, 439, 3016
- Mehdipour, M., Branduardi-Raymont, G., Kaastra, J. S., et al. 2011, *A&A*, 534, A39
- Mehdipour, M., Kaastra, J. S., Costantini, E., et al. 2018, *A&A*, 615, A72
- Mehdipour, M., Kaastra, J. S., Kriss, G. A., et al. 2015, *A&A*, 575, A22
- Mehdipour, M., Kriss, G. A., Kaastra, J. S., Costantini, E., & Mao, J. 2023, *ApJ*, 952, L5
- Middei, R., Bianchi, S., Cappi, M., et al. 2018, *A&A*, 615, A163
- Middei, R., Bianchi, S., Petrucci, P. O., et al. 2019a, *MNRAS*, 483, 4695
- Middei, R., Bianchi, S., Petrucci, P. O., et al. 2019b, *MNRAS*, 483, 4695
- Middei, R., Petrucci, P. O., Bianchi, S., et al. 2020, *A&A*, 640, A99
- Mishra, B., Begelman, M. C., Armitage, P. J., & Simon, J. B. 2020, *MNRAS*, 492, 1855
- Motta, S., Belloni, T., & Homan, J. 2009, *MNRAS*, 400, 1603
- Nayakshin, S. 2000, *ApJ*, 540, L37
- Nemmen, R. S., Georganopoulos, M., Guiriec, S., et al. 2012, *Science*, 338, 1445
- Noda, H. & Done, C. 2018, *MNRAS*, 480, 3898
- Noda, H., Makishima, K., Nakazawa, K., et al. 2013, *PASJ*, 65, 4
- Noda, H., Makishima, K., Yamada, S., et al. 2011, *PASJ*, 63, S925
- Page, K. L., Schartel, N., Turner, M. J. L., & O'Brien, P. T. 2004, *MNRAS*, 352, 523
- Pal, I., Stalin, C. S., Chatterjee, R., & Agrawal, V. K. 2023, *Journal of Astrophysics and Astronomy*, 44, 87
- Petrucci, P. O., Gronkiewicz, D., Rozanska, A., et al. 2020, *A&A*, 634, A85
- Petrucci, P. O., Paltani, S., Malzac, J., et al. 2013, *A&A*, 549, A73
- Petrucci, P. O., Ursini, F., De Rosa, A., et al. 2018, *A&A*, 611, A59
- Porquet, D., Hagen, S., Grosso, N., et al. 2024, *A&A*, 681, A40
- Porquet, D., Reeves, J. N., Matt, G., et al. 2018, *A&A*, 609, A42
- Pravdo, S. H., Nugent, J. J., Nousek, J. A., et al. 1981, *ApJ*, 251, 501
- Rees, M. J. 1984, *ARA&A*, 22, 471
- Ricci, C. & Trakhtenbrot, B. 2023, *Nature Astronomy*, 7, 1282
- Ricci, C., Trakhtenbrot, B., Koss, M. J., et al. 2017, *ApJS*, 233, 17
- Różańska, A. & Czerny, B. 2000a, *MNRAS*, 316, 473
- Różańska, A. & Czerny, B. 2000b, *A&A*, 360, 1170
- Różańska, A., Dumont, A. M., Czerny, B., & Collin, S. 2002, *MNRAS*, 332, 799
- Różańska, A., Goosmann, R., Dumont, A. M., & Czerny, B. 2006, *A&A*, 452, 1
- Różańska, A., Malzac, J., Belmont, R., Czerny, B., & Petrucci, P. O. 2015, *A&A*, 580, A77
- Schurch, N. J. & Done, C. 2008, *MNRAS*, 386, L1
- Steenbrugge, K. C., Kaastra, J. S., Blustin, A. J., et al. 2003, *A&A*, 408, 921

- Strüder, L., Aschenbach, B., Bräuninger, H., et al. 2001, *A&A*, 375, L5  
Tagliacozzo, D., Marinucci, A., Ursini, F., et al. 2023, *MNRAS*, 525, 4735  
Takeuchi, S., Ohsuga, K., & Mineshige, S. 2010, *PASJ*, 62, L43  
Tripathi, P., Dewangan, G. C., Papadakis, I. E., & Singh, K. P. 2021, *ApJ*, 915, 25  
Turner, N. J., Stone, J. M., Krolik, J. H., & Sano, T. 2003, *ApJ*, 593, 992  
Ursini, F., Petrucci, P. O., Matt, G., et al. 2018, *MNRAS*, 478, 2663  
Vaia, B., Ursini, F., Matt, G., et al. 2024, arXiv e-prints, arXiv:2405.13479  
Veronese, S., Vignali, C., Severgnini, P., Matzeu, G. A., & Cignoni, M. 2023, arXiv e-prints, arXiv:2312.07663  
Waddell, S. G. H., Nandra, K., Buchner, J., et al. 2023, arXiv e-prints, arXiv:2306.00961  
Wielgus, M., Lančová, D., Straub, O., et al. 2022, *MNRAS*, 514, 780  
Willingale, R., Starling, R. L. C., Beardmore, A. P., Tanvir, N. R., & O'Brien, P. T. 2013, *MNRAS*, 431, 394  
Xiang, X., Ballantyne, D. R., Bianchi, S., et al. 2022, *MNRAS*, 515, 353  
Xu, Y., García, J. A., Walton, D. J., et al. 2021, *ApJ*, 913, 13  
Yuan, F. & Narayan, R. 2014, *ARA&A*, 52, 529  
Zdziarski, A. A., Johnson, W. N., & Magdziarz, P. 1996, *MNRAS*, 283, 193  
Zoghbi, A. & Miller, J. M. 2023, *ApJ*, 957, 69  
Życki, P. T., Done, C., & Smith, D. A. 1999, *MNRAS*, 309, 561



## Appendix A: Impact of warm absorber

The warm ionized gas located on the line of sight towards the nucleus may absorb the soft X-ray continuum and therefore affect our analysis. The only way to eliminate the influence of eventual absorption is to implement CLOUDY multiplicative model component as indicated by Eq. 7. We do it in our automatic fitting procedure, and also manually for several heavily absorbed sources, as described above. As presented in Fig. A.1, a significant number of sources shows strong ionized host galaxy absorption with mean  $\log N_{\text{H}}^{\text{CL}} = 21.23 \pm 0.76$  and  $\log \xi_{\text{CL}} = 2.02 \pm 0.68$ . Best fitted values of the warm absorber model can be found in Table D.2, where second column is the column density third column is the ionization parameter. As mentioned in P18, the use of CLOUDY multiplicative table model is only to improve the fit statistic. Besides a few heavily obscured sources it has an insignificant effect on other parameter values. Nevertheless to ensure ourselves, we have repeated the entire fitting process without the CLOUDY table model which resulted in stronger residuals around 0.5-2 keV. However, trends among  $\tau_{\text{cor}}$ ,  $q_{\text{h}}$  and  $\Gamma_{\text{hc}}$  were approximately maintained, albeit with larger uncertainties.

As pointed out in Gierliński & Done (2004), complex absorption alone can reproduce shape of soft-excess, meaning that the interpretation of warm corona properties for heavily absorbed sources is not straightforward. Thus, a more accurate description of the complex absorption in these sources is necessary, requiring to construct new warm absorber model which is beyond the scope of this work.

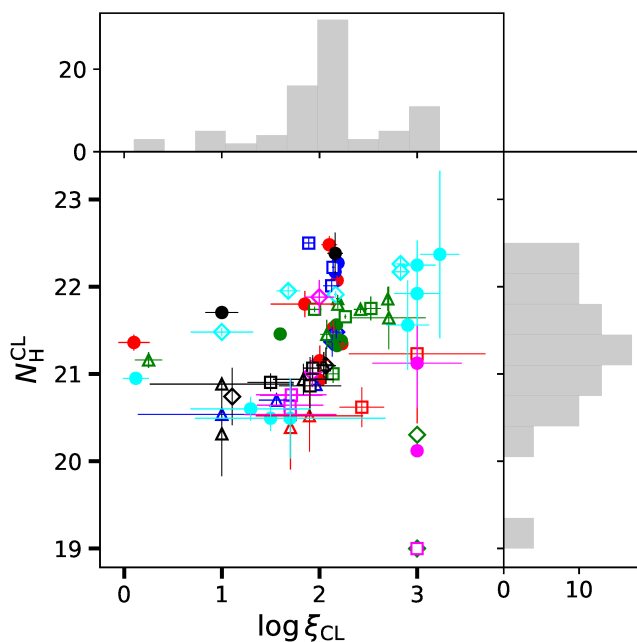


Fig. A.1: Scatter plot showing the best fitted hydrogen column density,  $N_{\text{H}}^{\text{CL}}$ , against ionization parameter,  $\xi_{\text{CL}}$ , of CLOUDY model. The distribution of their values is shown as grey histograms. Different symbols associated with sources are the same as in Fig. 6.

## Appendix B: Pearson's correlations and their MCMC simulations

In order to assess the robustness of strength of correlation estimated using Pearson's method (Fig. 6), we performed MCMC

simulations and obtained distribution of correlation strength indicator denoted by  $r$ -value and the rejection probability denoted by  $p$ -value. We performed  $10^6$  simulations by randomly sampling all the 82 data points within their error-bars and calculated Pearson's  $r$  and  $p$ -value for all  $10^6$  simulations. The results are shown in Fig. B.1. On the left panel, distribution of  $r$ -value is shown, which is characterised by a singly peaked approximate Gaussian shape. The mean, 5<sup>th</sup> & 95<sup>th</sup> percentiles are indicated in red vertical lines. On the right panel, their corresponding  $p$ -value distributions are shown. A  $p$ -value less than 0.05 is globally accepted as indication of high rejection probability of null hypothesis or highly significant estimation of any quantity. We normalized the y-axis for all plots. Fig. B.1 (left panel), showing uni-modal distribution of  $r$ -values indicates weak correlation strength of the primary warm corona properties with  $\Gamma_{\text{hc}}$ , but at high significance level of  $\gg 99\%$  (right panel).

## Appendix C: Impact of RELXILL- A prototypical case

Several AGNs have shown signatures of a broad iron  $K\alpha$  line (equivalent width  $\sim 420$ -560 eV) and is best described by relativistic reflection models. One such model is RELXILL. It takes into account the effects of strong gravity on reflected emission close to central black hole. However, often it is difficult to separate a broad component of iron line from the continuum, which is a key requirement to infer physical properties such as spin of black hole ( $a$ ), inner disk radius ( $R_{\text{in}}$ ) and emissivity. As shown by Guainazzi et al. (2006), about 200,000 counts in the hard X-ray band are necessary to ensure the presence of such broad features. To test relativistic effects on warm corona emission, we fit the *XMM-Newton* EPIC-pn spectra of a prototypical source-1H0416-577 which host broad iron lines and is well described by relativistic models (Jiang et al. 2019a). 1H0419-577 displayed a broad Fe  $K\alpha$  feature when the source was at a high flux state (Jiang et al. 2019a) in 2010 corresponding to ObsID: 0604720301. We replaced the XILLVER component with a basic flavour of RELXILL to study its effect on warm corona properties as well as inferring properties of inner accretion disk.

We obtained a better fit with the new model, where  $\Delta\chi^2=15$  for 5 extra degrees of freedom. During the fitting procedure, emissivity values were kept frozen at 5 and the break radius at  $50 R_{\text{g}}$  since they could not be restricted. The high energy cutoff was fixed at 300 keV and the model output was set to reflected emission only. With a F-statistic value of 2.69 and  $p$ -value of 0.02, however, this is not a highly significant improvement over the original model described in Sect. 2. As shown in Table C.1, the TiTAN/NOAR normalization reduced slightly due to mild contribution of RELXILL to the soft-excess (Fig. C.1). Comparing the best fit results from Table 3, there was negligible impact on the  $\tau_{\text{cor}}$  and  $\log q_{\text{h}}$  of warm corona. Given the limited energy range, strong constraints on  $R_{\text{in}}$ ,  $i$  and iron abundance ( $A_{\text{Fe}}$ ) could not be obtained. In addition, RELXILL is a heavy model and has a large convergence time during the fitting process and MCMC runs. Thus, in the current scenario, XILLVER can adequately describe the EPIC-pn spectra of majority of sources in our sample (describing the reflected emission below 10 keV) at a lower computation time.

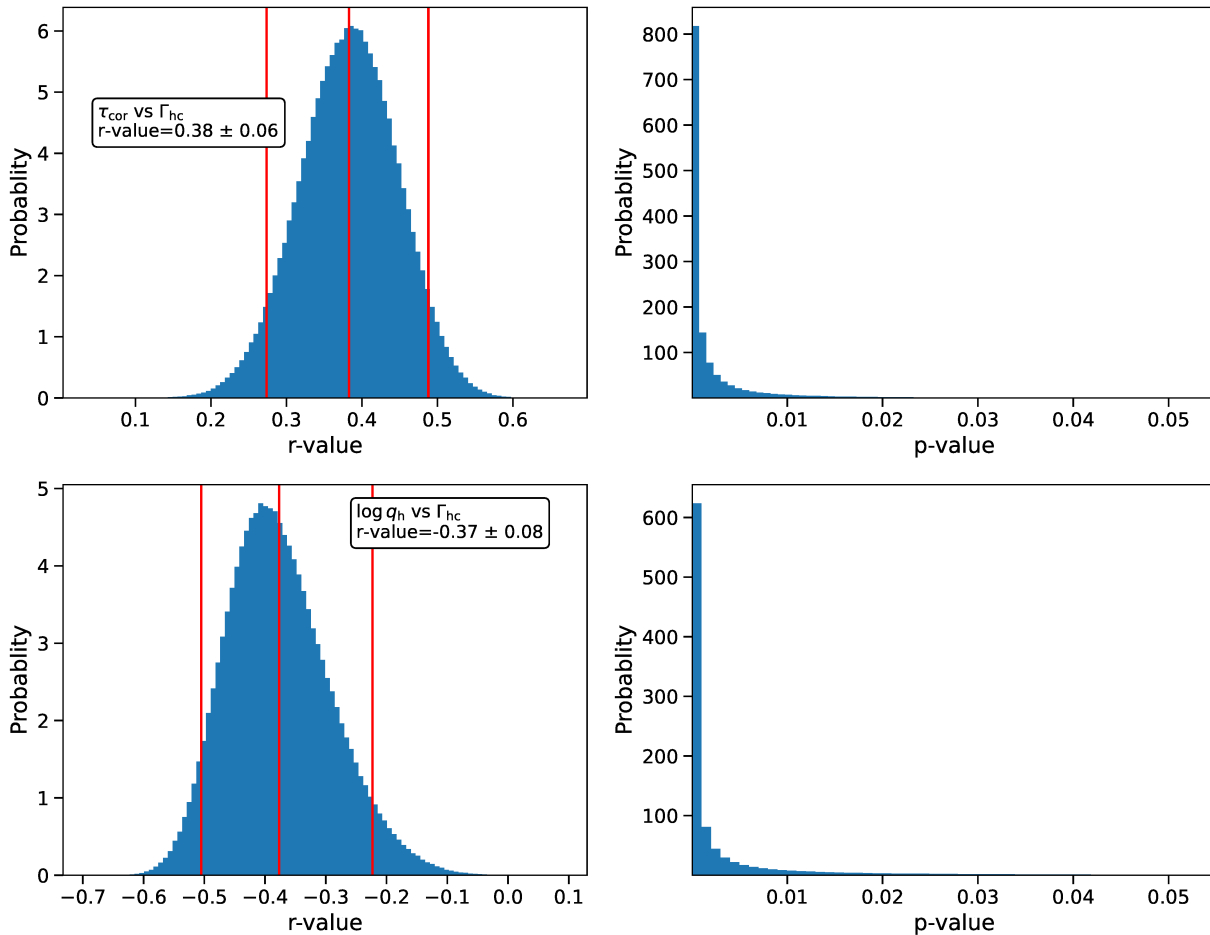


Fig. B.1: MCMC simulations showing the distribution of Pearson's r-value (left panel) and null hypothesis p-value (right panel) for warm corona optical depth  $\tau_{\text{cor}}$  and  $\log q_h$  vs the  $\Gamma_{\text{hc}}$ .

Table C.1: All best fitted parameters of the modified model as described in Appendix C applied to the source 1H0419-577 (ObsID: 0604720301).

Model	Parameter	1H0419-577 ObsID: 0604720301
WA	$\log \xi^{\text{CL}}$	$1.89 \pm 0.18$
	$\log N_{\text{H}}^{\text{CL}}$	$20.74 \pm 0.13$
zgauss	E (keV)	$0.537 \pm 0.005$
	$\sigma$ (eV)	1.00*
	Norm ( $\times 10^{-4}$ )	$2.12 \pm 0.52$
nthComp	$\Gamma_{\text{hc}}$	$1.66 \pm 0.11$
	Norm ( $\times 10^{-3}$ )	$2.68 \pm 0.65$
TiTAN/NOAR	$\tau_{\text{cor}}$	$17.87 \pm 1.49$
	$\log q_h$	$-22.33 \pm 0.09$
	Norm ( $\times 10^{-7}$ )	$1.75 \pm 0.12$
RELXILL	$a$	$0.99 \pm 0.11$
	$R_{\text{in}}$ (in $R_g$ )	$-4.95 \pm 6.50$
	$i$ (degrees)	$30.46 \pm 5.55$
	$A_{\text{Fe}}$	$0.50 \pm 0.45$
	$\log \xi$	$1.41 \pm 0.38$
	Norm ( $\times 10^{-5}$ )	$7.22 \pm 2.08$

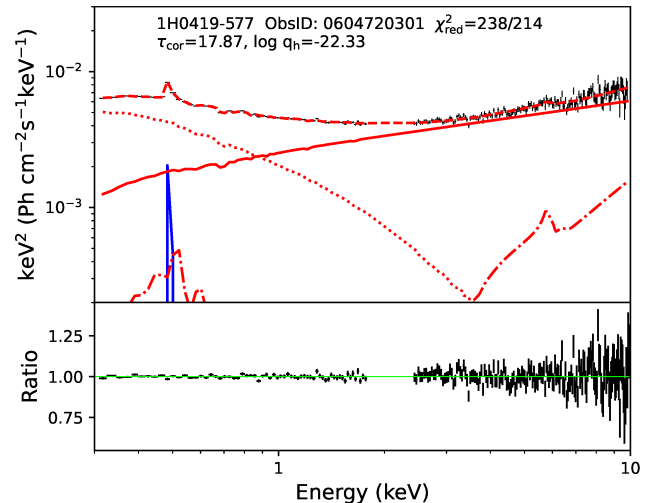


Fig. C.1: Example of unfolded best fit model to 1H0419-577 (ObsID: 0604720301) using relativistic reflection model as described in Appendix C and data/model ratio. The data are in black crosses. RELXILL model is represented by dashed-dotted line, NTHCOMP by solid line is and TiTAN/NOAR by dotted line. A narrow Gaussian at 0.537 keV is shown as blue solid line.

**Appendix D: Additional best fitted parameters**

Table D.1: All best fitted parameters for ZPCFABS model used to fit spectra of Mrk 335 described in Sect. 5.1 in the main paper

Model	Parameter	ObsID		
		0510010701	0600540501	0600540601
zpcfabs	$\log N_{\text{H}}$	$23.05 \pm 0.87$	$22.69 \pm 0.52$	19*
	$C_{\text{cov}} (\%)$	$90.64 \pm 0.03$	$25.30 \pm 0.02$	95*
XILLVER	$\log \xi_{\text{X}}$	0.00*	$1.21 \pm 0.05$	$1.33 \pm 0.07$

**Notes:**

\*denotes the value of parameter was unconstrained hence it was kept frozen.

Table 3: List of physically important quantities associated with our sample.

Source										[ $\times 10^{-11}$ ]
ObsID	$\chi^2_{\text{red}}$	$\frac{L_{\text{Bol}}}{L_{\text{Edd}}}$	HR	$\Gamma_{\text{hc}}$	$\log q_{\text{h}}$	$\tau_{\text{cor}}$	$\chi$	SE		$F_{0.3-10}$
1H0419-577										
112600401	0.94	0.195	$-0.20 \pm 0.04$	$1.87 \pm 0.08$	$-22.51 \pm 0.06$	$28.09 \pm 2.48$	$1.71 \pm 0.02$	$0.70 \pm 0.37$		$3.85 \pm 0.27$
148000201	1.32	0.098	$0.45 \pm 0.06$	$1.70 \pm 0.06$	$-22.07 \pm 0.38$	$16.65 \pm 5.77$	$1.71 \pm 0.07$	$5.75 \pm 2.75$		$1.05 \pm 0.07$
148000301	1.30	0.097	$0.21 \pm 0.06$	$1.71 \pm 0.06$	$-22.37 \pm 0.21$	$20.04 \pm 3.87$	$1.61 \pm 0.05$	$1.47 \pm 0.71$		$1.27 \pm 0.09$
148000401	1.03	0.290	$-0.06 \pm 0.03$	$1.76 \pm 0.02$	$-22.56 \pm 0.05$	$13.72 \pm 1.52$	$1.13 \pm 0.05$	$1.77 \pm 0.22$		$2.34 \pm 0.11$
148000501	1.19	0.166	$-0.02 \pm 0.03$	$1.55 \pm 0.08$	$-22.05 \pm 0.21$	$7.42 \pm 2.04$	$1.14 \pm 0.11$	$3.63 \pm 1.55$		$2.03 \pm 0.14$
148000601	1.08	0.102	$0.02 \pm 0.03$	$1.66 \pm 0.18$	$-22.22 \pm 0.41$	$14.55 \pm 5.07$	$1.52 \pm 0.12$	$1.45 \pm 0.45$		$1.89 \pm 0.13$
604720301	1.15	0.156	$-0.17 \pm 0.01$	$1.56 \pm 0.04$	$-22.34 \pm 0.02$	$19.35 \pm 1.51$	$1.61 \pm 0.01$	$1.65 \pm 0.71$		$3.16 \pm 0.07$
604720401	1.15	0.128	$-0.14 \pm 0.01$	$1.59 \pm 0.04$	$-22.38 \pm 0.03$	$18.47 \pm 0.69$	$1.56 \pm 0.01$	$1.69 \pm 0.44$		$2.91 \pm 0.14$
ESO198-G24										
067190101	1.29	0.013	$0.004 \pm 0.014$	$1.79 \pm 0.06$	$-22.41 \pm 0.20$	$30.00 \pm 13.25$	$1.78 \pm 0.08$	$0.21 \pm 0.03$		$2.55 \pm 0.01$
112910101	1.20	0.009	$0.01 \pm 0.04$	$1.80 \pm 0.24$	$-21.75 \pm 0.55$	$12.75 \pm 10.00$	$1.76 \pm 0.15$	$0.20 \pm 0.06$		$1.98 \pm 0.05$
305370101	1.11	0.012	$0.04 \pm 0.01$	$1.03 \pm 0.23$	$-21.79 \pm 0.10$	$18.24 \pm 1.95$	$1.86 \pm 0.01$	$13.83 \pm 2.96$		$1.949 \pm 0.005$
HB890405-123										
202210301	0.90	-	$-0.09 \pm 0.02$	$1.78 \pm 0.07$	$-22.34 \pm 0.08$	$16.46 \pm 1.54$	$1.51 \pm 0.03$	$0.67 \pm 0.17$		$0.952 \pm 0.003$
202210401	1.00	-	$-0.08 \pm 0.02$	$1.66 \pm 0.05$	$-21.92 \pm 0.14$	$9.31 \pm 1.66$	$1.46 \pm 0.06$	$1.22 \pm 0.37$		$0.975 \pm 0.007$
HE1029-1401										
110950101	1.12	0.090	$-0.19 \pm 0.04$	$1.69 \pm 0.12$	$-21.73 \pm 0.37$	$7.75 \pm 3.49$	$1.50 \pm 0.14$	$2.57 \pm 0.55$		$3.25 \pm 0.15$
203770101	1.16	0.102	$-0.13 \pm 0.01$	$1.79 \pm 0.04$	$-22.43 \pm 0.03$	$25.02 \pm 0.82$	$1.70 \pm 0.01$	$1.01 \pm 0.31$		$4.85 \pm 0.01$
IRASFI2397+3333										
202180201	1.21	0.615	$-0.28 \pm 0.02$	$1.95 \pm 0.12$	$-21.87 \pm 0.13$	$8.48 \pm 1.34$	$1.44 \pm 0.06$	$4.07 \pm 1.38$		$1.301 \pm 0.001$
202180301	1.00	0.270	$-0.21 \pm 0.05$	$2.01 \pm 0.49$	$-22.35 \pm 0.23$	$16.41 \pm 2.93$	$1.49 \pm 0.06$	$0.81 \pm 0.30$		$1.04 \pm 0.05$
LBQS1228+1116										
306630101	0.88	-	$-0.22 \pm 0.04$	$1.81 \pm 0.12$	$-22.43 \pm 0.06$	$30.00 \pm 6.42$	$1.78 \pm 0.04$	$1.08 \pm 0.28$		$0.28 \pm 0.01$
306630201	0.97	-	$-0.22 \pm 0.03$	$1.84 \pm 0.10$	$-22.42 \pm 0.06$	$30.00 \pm 5.69$	$1.78 \pm 0.04$	$1.01 \pm 0.33$		$0.30 \pm 0.01$
MRK279										
302480401	1.23	0.127	$-0.13 \pm 0.01$	$1.83 \pm 0.03$	$-22.45 \pm 0.04$	$27.34 \pm 1.08$	$1.73 \pm 0.01$	$0.51 \pm 0.13$		$6.04 \pm 0.00$
302480501	1.28	0.120	$-0.06 \pm 0.01$	$1.76 \pm 0.02$	$-22.48 \pm 0.03$	$30.00 \pm 2.54$	$1.75 \pm 0.02$	$0.48 \pm 0.12$		$5.57 \pm 0.39$
302480601	0.98	0.121	$-0.12 \pm 0.01$	$1.84 \pm 0.04$	$-22.46 \pm 0.05$	$27.49 \pm 1.63$	$1.73 \pm 0.01$	$0.49 \pm 0.14$		$5.59 \pm 0.26$
MRK335										
510010701	1.25	0.167	$0.19 \pm 0.05$	$2.53 \pm 0.10$	$-22.52 \pm 0.09$	$30.0 \pm 10.81$	$1.73 \pm 0.08$	$3.58 \pm 1.70$		$0.61 \pm 0.04$
600540501	1.21	0.186	$-0.09 \pm 0.02$	$1.92 \pm 0.03$	$-22.08 \pm 0.05$	$6.70 \pm 2.49$	$1.00 \pm 0.18$	$0.63 \pm 0.19$		$1.28 \pm 0.03$
600540601	1.60	0.172	$0.04 \pm 0.02$	$1.98 \pm 0.02$	$-22.52 \pm 0.03$	$16.97 \pm 2.83$	$1.36 \pm 0.03$	$0.53 \pm 0.13$		$1.00 \pm 0.02$
MRK509										
130720101	1.24	0.056	$0.05 \pm 0.01$	$1.69 \pm 0.04$	$-22.46 \pm 0.05$	$23.00 \pm 1.30$	$1.63 \pm 0.02$	$0.62 \pm 0.15$		$5.92 \pm 0.14$
601390201	1.17	0.127	$-0.14 \pm 0.01$	$1.69 \pm 0.03$	$-22.16 \pm 0.06$	$13.16 \pm 0.73$	$1.50 \pm 0.02$	$1.69 \pm 0.35$		$10.80 \pm 0.25$
601390301	1.29	0.123	$-0.15 \pm 0.01$	$1.72 \pm 0.03$	$-22.19 \pm 0.08$	$13.70 \pm 0.57$	$1.50 \pm 0.01$	$1.77 \pm 0.38$		$11.26 \pm 0.26$
601390401	1.29	0.157	$-0.20 \pm 0.01$	$1.60 \pm 0.02$	$-22.11 \pm 0.08$	$12.81 \pm 0.77$	$1.52 \pm 0.02$	$2.46 \pm 1.05$		$13.41 \pm 0.93$
601390501	1.36	0.176	$-0.22 \pm 0.01$	$1.61 \pm 0.03$	$-22.23 \pm 0.03$	$12.97 \pm 0.43$	$1.42 \pm 0.02$	$2.65 \pm 0.59$		$11.29 \pm 0.26$
601390601	1.25	0.197	$-0.25 \pm 0.01$	$1.73 \pm 0.03$	$-22.28 \pm 0.03$	$13.74 \pm 0.46$	$1.43 \pm 0.01$	$3.47 \pm 0.74$		$13.84 \pm 0.65$
601390701	1.26	0.157	$-0.18 \pm 0.01$	$1.72 \pm 0.02$	$-22.25 \pm 0.11$	$14.91 \pm 1.08$	$1.51 \pm 0.02$	$1.69 \pm 0.36$		$13.61 \pm 0.32$
601390801	1.21	0.146	$-0.19 \pm 0.01$	$1.63 \pm 0.02$	$-22.12 \pm 0.07$	$13.14 \pm 0.66$	$1.53 \pm 0.02$	$2.05 \pm 0.69$		$13.01 \pm 0.30$
601390901	1.26	0.131	$-0.16 \pm 0.01$	$1.61 \pm 0.04$	$-22.03 \pm 0.07$	$12.52 \pm 0.92$	$1.58 \pm 0.02$	$2.65 \pm 1.05$		$13.49 \pm 0.31$
601391001	1.24	0.135	$-0.18 \pm 0.01$	$1.78 \pm 0.02$	$-22.3 \pm 0.04$	$15.09 \pm 0.55$	$1.48 \pm 0.01$	$1.69 \pm 0.44$		$12.24 \pm 1.42$
601391101	1.18	0.134	$-0.14 \pm 0.01$	$1.64 \pm 0.03$	$-22.10 \pm 0.08$	$12.78 \pm 1.00$	$1.54 \pm 0.03$	$2.04 \pm 0.43$		$12.86 \pm 0.30$
MRK590										
109130301	0.87	0.008	$0.05 \pm 0.05$	$1.62 \pm 0.31$	$-22.31 \pm 0.36$	$30.0 \pm 22.25$	$1.83 \pm 0.11$	$0.62 \pm 0.29$		$0.90 \pm 0.06$
201020201	1.12	0.009	$0.07 \pm 0.02$	$1.53 \pm 0.88$	$-21.57 \pm 0.06$	$17.8 \pm 1.17$	$1.91 \pm 0.01$	$2.57 \pm 0.29$		$1.23 \pm 0.03$
NGC4593										
059830101	1.49	0.075	$-0.03 \pm 0.01$	$1.87 \pm 0.04$	$-22.45 \pm 0.04$	$20.84 \pm 2.85$	$1.57 \pm 0.01$	$0.45 \pm 0.12$		$8.18 \pm 0.19$
109970101	1.35	0.053	$-0.05 \pm 0.02$	$1.55 \pm 0.07$	$-21.62 \pm 0.27$	$9.35 \pm 2.80$	$1.69 \pm 0.07$	$2.45 \pm 0.83$		$8.21 \pm 0.19$
740920201	1.42	0.056	$0.05 \pm 0.02$	$1.82 \pm 0.03$	$-22.20 \pm 0.07$	$16.50 \pm 6.56$	$1.61 \pm 0.04$	$0.89 \pm 0.24$		$4.25 \pm 0.10$
740920301	1.10	0.025	$0.15 \pm 0.03$	$1.70 \pm 0.02$	$-21.97 \pm 0.05$	$9.84 \pm 3.92$	$1.45 \pm 0.04$	$0.72 \pm 0.24$		$2.35 \pm 0.11$
740920401	1.47	0.029	$0.15 \pm 0.02$	$1.65 \pm 0.03$	$-22.12 \pm 0.79$	$13.75 \pm 10.21$	$1.56 \pm 0.23$	$0.52 \pm 0.13$		$2.54 \pm 0.06$
740920501	1.20	0.044	$0.02 \pm 0.01$	$1.59 \pm 0.12$	$-22.13 \pm 0.23$	$17.02 \pm 2.39$	$1.68 \pm 0.03$	$1.44 \pm 0.49$		$5.30 \pm 0.61$
740920601	1.28	0.043	$0.01 \pm 0.01$	$1.71 \pm 0.12$	$-22.19 \pm 0.23$	$16.55 \pm 2.78$	$1.63 \pm 0.05$	$0.63 \pm 0.19$		$5.12 \pm 0.83$
NGC7469										
112170101	1.17	0.021	$-0.10 \pm 0.02$	$1.97 \pm 0.04$	$-22.54 \pm 0.06$	$30.00 \pm 5.13$	$1.72 \pm 0.04$	$0.38 \pm 0.15$		$6.01 \pm 0.14$
112170301	1.06	0.024	$-0.16 \pm 0.02$	$2.01 \pm 0.02$	$-22.44 \pm 0.06$	$23.65 \pm 1.15$	$1.66 \pm 0.01$	$0.97 \pm 0.15$		$7.05 \pm 1.15$
207090101	1.33	0.025	$-0.16 \pm 0.01$	$1.58 \pm 0.02$	$-21.98 \pm 0.08$	$12.50 \pm 1.19$	$1.61 \pm 0.03$	$3.89 \pm 1.02$		$7.33 \pm 0.67$
207090201	1.21	0.024	$-0.08 \pm 0.01$	$1.88 \pm 0.02$	$-22.47 \pm 0.04$	$27.43 \pm 1.20$	$1.72 \pm 0.01$	$0.53 \pm 0.14$		$6.81 \pm 0.62$
PG0804+761										
605110101	0.97	0.402	$-0.32 \pm 0.02$	$1.37 \pm 0.07$	$-21.73 \pm 0.15$	$7.52 \pm 1.41$	$1.48 \pm 0.06$	$7.41 \pm 2.75$		$3.23 \pm 0.01$
605110201	1.12	0.434	$-0.37 \pm 0.03$	$1.31 \pm 0.11$	$-21.74 \pm 0.13$	$7.75 \pm 1.34$	$1.49 \pm 0.06$	$11.63 \pm 2.52$		$2.51 \pm 0.06$
PG0844+349										

Table 3: continued.

Source										[ $\times 10^{-11}$ ]
ObsID	$\chi_{\text{red}}^2$	$\frac{L_{\text{Bol}}}{L_{\text{Edd}}}$	HR	$\Gamma_{\text{hc}}$	$\log q_{\text{h}}$	$\tau_{\text{cor}}$	$\chi$	SE		$F_{0.3-10}$
103660201	1.16	0.107	$-0.35 \pm 0.03$	$2.06 \pm 0.09$	$-22.52 \pm 0.04$	$26.60 \pm 1.52$	$1.67 \pm 0.01$	$0.91 \pm 0.36$		$1.64 \pm 0.04$
554710101	1.05	0.085	$0.20 \pm 0.10$	$1.19 \pm 0.13$	$-22.55 \pm 0.05$	$30.00 \pm 7.75$	$1.72 \pm 0.06$	$3.23 \pm 0.69$		$0.193 \pm 0.001$
PG1116+215										
201940101	1.02	0.384	$-0.33 \pm 0.02$	$1.83 \pm 0.09$	$-22.4 \pm 0.04$	$21.86 \pm 0.85$	$1.64 \pm 0.01$	$1.58 \pm 0.48$		$0.991 \pm 0.002$
201940201	1.04	0.392	$-0.35 \pm 0.06$	$2.11 \pm 0.13$	$-22.54 \pm 0.10$	$27.78 \pm 4.47$	$1.69 \pm 0.04$	$0.53 \pm 0.11$		$1.06 \pm 0.01$
554380101	1.06	0.404	$-0.34 \pm 0.02$	$1.61 \pm 0.34$	$-22.27 \pm 0.18$	$16.55 \pm 2.18$	$1.57 \pm 0.04$	$3.04 \pm 0.91$		$1.42 \pm 0.07$
554380201	1.16	0.373	$-0.22 \pm 0.02$	$1.45 \pm 0.14$	$-22.03 \pm 0.21$	$12.18 \pm 2.62$	$1.55 \pm 0.07$	$3.01 \pm 0.79$		$1.12 \pm 0.05$
554380301	1.16	0.425	$-0.28 \pm 0.03$	$1.43 \pm 0.07$	$-21.75 \pm 0.17$	$7.50 \pm 1.62$	$1.46 \pm 0.07$	$5.01 \pm 1.10$		$0.91 \pm 0.02$
PG1351+640										
205390301	1.08	0.269	$-0.24 \pm 0.05$	$1.98 \pm 0.14$	$-22.53 \pm 0.05$	$28.26 \pm 2.22$	$1.70 \pm 0.02$	$1.64 \pm 0.34$		$0.16 \pm 0.01$
556230201	1.07	0.238	$0.49 \pm 0.12$	$2.15 \pm 0.22$	$-21.59 \pm 0.29$	$24.1 \pm 15.28$	$1.95 \pm 0.03$	$2.68 \pm 0.81$		$0.067 \pm 0.004$
PG1402+261										
400200101	0.99	0.485	$-0.35 \pm 0.04$	$2.03 \pm 0.14$	$-22.49 \pm 0.07$	$21.46 \pm 1.60$	$1.57 \pm 0.02$	$0.97 \pm 0.25$		$0.52 \pm 0.01$
400200201	1.09	0.438	$-0.32 \pm 0.06$	$1.71 \pm 0.22$	$-21.59 \pm 0.42$	$6.52 \pm 3.97$	$1.93 \pm 0.03$	$0.32 \pm 0.06$		$0.39 \pm 0.01$
PG1440+356										
005010101	1.27	0.635	$-0.51 \pm 0.04$	$2.17 \pm 0.10$	$-22.53 \pm 0.04$	$22.50 \pm 0.99$	$1.57 \pm 0.01$	$4.07 \pm 1.07$		$1.36 \pm 0.03$
005010201	1.01	0.625	$-0.53 \pm 0.06$	$2.00 \pm 0.19$	$-22.51 \pm 0.05$	$21.13 \pm 1.15$	$1.54 \pm 0.02$	$2.34 \pm 0.61$		$1.18 \pm 0.05$
005010301	1.10	0.458	$-0.51 \pm 0.05$	$2.13 \pm 0.18$	$-22.49 \pm 0.06$	$20.59 \pm 1.20$	$1.54 \pm 0.02$	$1.40 \pm 0.55$		$0.72 \pm 0.02$
107660201	0.76	0.635	$-0.58 \pm 0.04$	$2.26 \pm 0.10$	$-22.56 \pm 0.03$	$25.86 \pm 1.05$	$1.63 \pm 0.01$	$1.32 \pm 0.50$		$1.26 \pm 0.05$
Q0056-363										
102040701	0.84	0.073	$-0.31 \pm 0.04$	$2.03 \pm 0.14$	$-22.45 \pm 0.10$	$24.20 \pm 3.11$	$1.67 \pm 0.03$	$0.68 \pm 0.25$		$0.80 \pm 0.02$
205680101	1.31	0.053	$-0.27 \pm 0.02$	$1.48 \pm 0.13$	$-22.07 \pm 0.10$	$14.24 \pm 1.11$	$1.62 \pm 0.02$	$4.69 \pm 1.00$		$0.790 \pm 0.002$
401930101	0.98	0.041	$-0.28 \pm 0.03$	$1.92 \pm 0.12$	$-22.41 \pm 0.07$	$24.18 \pm 1.83$	$1.69 \pm 0.02$	$0.91 \pm 0.36$		$0.74 \pm 0.02$
RE1034+396										
109070101	1.25	1.519	$-0.79 \pm 0.06$	$2.41 \pm 0.14$	$-22.65 \pm 0.01$	$22.40 \pm 0.64$	$1.46 \pm 0.01$	$4.34 \pm 1.47$		$0.97 \pm 0.02$
506440101	1.11	1.500	$-0.79 \pm 0.02$	$2.42 \pm 0.07$	$-22.65 \pm 0.01$	$24.85 \pm 0.42$	$1.53 \pm 0.01$	$3.60 \pm 1.10$		$0.976 \pm 0.002$
561580201	1.49	1.698	$-0.84 \pm 0.03$	$2.25 \pm 0.09$	$-22.77 \pm 0.02$	$30.00 \pm 1.10$	$1.57 \pm 0.01$	$10.22 \pm 2.19$		$1.404 \pm 0.001$
655310101	1.12	1.804	$-0.74 \pm 0.04$	$2.14 \pm 0.10$	$-22.72 \pm 0.01$	$22.23 \pm 0.76$	$1.39 \pm 0.01$	$5.67 \pm 1.47$		$1.05 \pm 0.02$
655310201	1.30	1.750	$-0.72 \pm 0.04$	$1.90 \pm 0.14$	$-22.61 \pm 0.01$	$18.46 \pm 0.56$	$1.34 \pm 0.01$	$8.71 \pm 2.39$		$0.96 \pm 0.02$
675440101	1.23	1.889	$-0.72 \pm 0.04$	$1.90 \pm 0.12$	$-22.65 \pm 0.01$	$18.36 \pm 0.98$	$1.29 \pm 0.02$	$12.06 \pm 3.10$		$1.09 \pm 0.03$
675440201	0.84	1.819	$-0.68 \pm 0.05$	$1.85 \pm 0.22$	$-22.63 \pm 0.01$	$19.3 \pm 0.71$	$1.36 \pm 0.01$	$9.12 \pm 2.39$		$1.05 \pm 0.02$
675440301	1.17	1.691	$-0.79 \pm 0.04$	$1.50 \pm 0.12$	$-22.73 \pm 0.01$	$29.98 \pm 1.30$	$1.60 \pm 0.01$	$14.45 \pm 3.10$		$1.66 \pm 0.04$
UGC3973										
103862101	1.32	0.027	$0.13 \pm 0.05$	$1.52 \pm 0.16$	$-21.99 \pm 0.59$	$11.29 \pm 8.20$	$1.54 \pm 0.23$	$3.16 \pm 0.67$		$2.30 \pm 0.16$
400070201	1.13	0.034	$-0.12 \pm 0.02$	$1.49 \pm 0.18$	$-21.93 \pm 0.15$	$13.42 \pm 2.24$	$1.68 \pm 0.04$	$7.41 \pm 1.94$		$5.68 \pm 0.13$
400070301	1.19	0.025	$0.06 \pm 0.02$	$2.29 \pm 0.05$	$-21.54 \pm 0.12$	$18.46 \pm 2.25$	$1.92 \pm 0.01$	$9.33 \pm 2.45$		$4.07 \pm 0.09$
400070401	1.21	0.028	$-0.01 \pm 0.02$	$1.30 \pm 0.10$	$-21.95 \pm 0.17$	$13.60 \pm 2.26$	$1.68 \pm 0.04$	$8.15 \pm 1.74$		$4.16 \pm 0.10$
502091001	1.43	0.025	$0.42 \pm 0.05$	$1.86 \pm 0.04$	$-22.31 \pm 0.11$	$22.00 \pm 5.08$	$1.70 \pm 0.06$	$0.57 \pm 0.17$		$1.06 \pm 0.02$

**Notes:**

The best fitted parameters—hot corona photon index ( $\Gamma_{\text{hc}}$ ), total internal heating ( $\log q_{\text{h}}$ ) and optical depth of warm corona ( $\tau_{\text{cor}}$ ) of the model-TBABS\*LOUDY\*(TITAN+NTHCOMP+XILLVER) as described in Sect. 2 are presented in columns 5-7 respectively.

Goodness of fit indicator- reduced Chi-square values ( $\chi_{\text{red}}^2$ ) are listed in second column.

Values of accretion rate ( $L_{\text{Bol}}/L_{\text{Edd}}$ ) were adopted from P18 are mentioned in the third column, where ‘-’ denotes missing values.

Hardness ratios (HR) were computed using count rates are listed in fourth column.

Dissipation factor ( $\chi$ ), were calculated a posteriori using Eqn 4 mentioned in eighth column.

Soft excess strength (SE) were calculated using Eq. 9 mentioned in ninth column.

$F_{0.3-10}$  is the un-absorbed flux in the energy range 0.3–10 keV, expressed in units of  $\text{ergs s}^{-1} \text{cm}^{-2}$ , mentioned in tenth column.



Table D.2: Additional best fitted parameters for all objects in our sample

Source ObsID	$\log N_{\text{H}}^{\text{CL}}$	$\log \xi_{\text{CL}}$	$[\times 10^{-3}]$ $N_{\text{hc}}$	$[\times 10^{-5}]$ $N_{\text{X}}$
1H0419-577				
112600401	$21.15 \pm 0.17$	$2.00 \pm 0.09$	$4.80 \pm 0.65$	$3.08 \pm 1.52$
148000201	$22.48 \pm 0.10$	$2.10 \pm 0.08$	$2.08 \pm 0.27$	$4.38 \pm 0.79$
148000301	$21.80 \pm 0.15$	$1.85 \pm 0.35$	$1.99 \pm 0.21$	$2.28 \pm 0.90$
148000401	$21.36 \pm 0.09$	$0.10 \pm 0.16$	$2.90 \pm 0.06$	$1.44 \pm 0.77$
148000501	$21.52 \pm 0.07$	$2.14 \pm 0.03$	$1.25 \pm 0.74$	$3.27 \pm 2.08$
148000601	$22.07 \pm 0.05$	$2.18 \pm 0.02$	$2.12 \pm 1.05$	$3.38 \pm 0.98$
604720301	$20.93 \pm 0.08$	$2.00 \pm 0.04$	$2.57 \pm 0.19$	$1.38 \pm 0.45$
604720401	$21.34 \pm 0.05$	$2.23 \pm 0.03$	$2.29 \pm 0.27$	$1.33 \pm 0.58$
ESO198-G24				
67190101	19.00*	3.00*	$3.46 \pm 0.56$	$1.63 \pm 0.51$
112910101	19.00*	3.00*	$2.68 \pm 1.57$	$4.24 \pm 1.03$
305370101	19.00*	3.00*	$0.22 \pm 0.14$	$10.26 \pm 7.22$
HB890405-123				
202210301	$20.51 \pm 0.41$	$1.89 \pm 0.54$	$1.10 \pm 0.17$	$0.76 \pm 0.25$
202210401	$20.38 \pm 0.48$	$1.70 \pm 1.29$	$0.86 \pm 0.09$	$0.71 \pm 0.27$
HE1029-1401				
110950101	$21.22 \pm 0.79$	$3.00 \pm 0.69$	$2.03 \pm 0.71$	$3.60 \pm 1.27$
203770101	$20.61 \pm 0.22$	$2.43 \pm 0.20$	$5.06 \pm 0.44$	$4.01 \pm 0.64$
IRASFI2397+3333				
202180201	$22.17 \pm 0.01$	$2.16 \pm 0.01$	$1.20 \pm 0.70$	$1.17 \pm 0.25$
202180301	$22.27 \pm 0.04$	$2.19 \pm 0.01$	$1.73 \pm 0.30$	$1.22 \pm 0.71$
LBQS1228+1116				
306630101	$21.36 \pm 0.16$	$2.13 \pm 0.09$	$0.30 \pm 0.07$	$0.30 \pm 0.13$
306630201	$21.47 \pm 0.12$	$2.17 \pm 0.06$	$0.33 \pm 0.07$	$0.37 \pm 0.12$
MRK279				
302480401	$20.88 \pm 0.07$	$1.96 \pm 0.04$	$7.68 \pm 0.51$	$8.52 \pm 0.73$
302480501	$20.70 \pm 0.07$	$1.56 \pm 0.18$	$6.91 \pm 0.31$	$7.79 \pm 0.66$
302480601	$20.53 \pm 0.11$	$1.00 \pm 0.85$	$7.19 \pm 0.60$	$9.52 \pm 0.96$
MRK335				
510010701	$22.50 \pm 0.05$	$1.89 \pm 0.06$	$3.31 \pm 1.03$	$6.22 \pm 2.63$
600540501	$22.01 \pm 0.07$	$2.12 \pm 0.08$	$2.27 \pm 0.19$	$4.92 \pm 0.36$
600540601	$22.22 \pm 0.05$	$2.14 \pm 0.01$	$1.70 \pm 0.06$	$3.50 \pm 0.20$
MRK509				
130720101	$21.56 \pm 0.05$	$2.17 \pm 0.02$	$6.87 \pm 0.57$	$9.68 \pm 1.04$
601390201	$21.32 \pm 0.03$	$2.18 \pm 0.02$	$8.99 \pm 0.88$	$10.73 \pm 0.90$
601390301	$21.36 \pm 0.03$	$2.16 \pm 0.01$	$9.68 \pm 1.53$	$13.44 \pm 1.01$
601390401	$21.45 \pm 0.02$	$1.59 \pm 0.01$	$9.25 \pm 0.99$	$14.95 \pm 0.92$
601390501	$21.37 \pm 0.03$	$2.15 \pm 0.02$	$8.05 \pm 1.46$	$11.32 \pm 1.02$
601390601	$21.38 \pm 0.03$	$2.15 \pm 0.02$	$7.86 \pm 0.66$	$12.63 \pm 0.94$
601390701	$21.39 \pm 0.03$	$2.19 \pm 0.01$	$11.58 \pm 2.87$	$12.56 \pm 1.16$
601390801	$21.37 \pm 0.03$	$2.18 \pm 0.01$	$9.85 \pm 1.38$	$13.97 \pm 0.95$
601390901	$21.37 \pm 0.03$	$2.22 \pm 0.01$	$8.47 \pm 1.17$	$13.17 \pm 1.04$
601391001	$21.35 \pm 0.03$	$2.17 \pm 0.01$	$11.48 \pm 1.54$	$12.91 \pm 0.93$
601391101	$21.39 \pm 0.02$	$2.18 \pm 0.01$	$9.62 \pm 1.12$	$13.64 \pm 0.96$
MRK590				
109130301	20.30*	3.00*	$0.88 \pm 0.63$	$4.82 \pm 1.24$
201020201	19.00*	3.00*	$0.01 \pm 0.29$	$4.14 \pm 5.09$
NGC4593				
59830101	$21.74 \pm 0.04$	$2.42 \pm 0.06$	$12.25 \pm 0.11$	$18.09 \pm 0.75$
109970101	$21.86 \pm 0.04$	$2.18 \pm 0.02$	$5.12 \pm 1.28$	$17.09 \pm 2.24$
740920201	$21.64 \pm 0.36$	$2.71 \pm 0.37$	$6.28 \pm 0.22$	$9.56 \pm 1.13$
740920301	$21.16 \pm 0.09$	$0.25 \pm 0.14$	$2.95 \pm 0.15$	$11.45 \pm 1.03$
740920401	$21.45 \pm 0.16$	$2.07 \pm 0.06$	$3.38 \pm 0.13$	$11.71 \pm 0.88$
740920501	$21.80 \pm 0.04$	$2.18 \pm 0.02$	$4.59 \pm 1.77$	$14.74 \pm 2.10$
740920601	$21.86 \pm 0.13$	$2.70 \pm 0.03$	$5.79 \pm 2.17$	$12.12 \pm 1.28$
NGC7469				
112170101	$21.75 \pm 0.13$	$2.52 \pm 0.10$	$8.75 \pm 0.52$	$13.05 \pm 1.35$
112170301	$21.74 \pm 0.03$	$1.95 \pm 0.07$	$9.91 \pm 0.20$	$10.79 \pm 1.12$
207090101	$21.65 \pm 0.05$	$2.26 \pm 0.01$	$3.52 \pm 0.46$	$12.76 \pm 1.12$
207090201	$21.00 \pm 0.10$	$2.14 \pm 0.04$	$9.08 \pm 0.41$	$8.91 \pm 0.47$
PG0804+761				
605110101	$20.12 \pm 3.24$	$3.00 \pm 3.00$	$0.95 \pm 0.17$	$3.28 \pm 1.02$
605110201	$21.12 \pm 0.51$	$3.00 \pm 0.45$	$0.52 \pm 0.15$	$5.83 \pm 1.47$
PG0844+349				

Table D.2: Continued.

Source ObsID	$\log N_{\text{H}}^{\text{CL}}$	$\log \xi_{\text{CL}}$	$[\times 10^{-3}]$ $N_{\text{hc}}$	$[\times 10^{-5}]$ $N_{\text{X}}$
103660201	$21.01 \pm 0.16$	$1.92 \pm 0.10$	$2.03 \pm 0.30$	$1.06 \pm 0.57$
554710101	$21.87 \pm 0.19$	$1.99 \pm 0.15$	$0.09 \pm 0.02$	$2.05 \pm 0.76$
PG1116+215				
201940101	$20.64 \pm 0.15$	$1.69 \pm 0.34$	$0.92 \pm 0.17$	$0.76 \pm 0.21$
201940201	19.00*	3.00*	$1.48 \pm 0.31$	$1.53 \pm 0.95$
554380101	$20.53 \pm 0.23$	$1.70 \pm 0.47$	$0.85 \pm 0.73$	$0.93 \pm 0.38$
554380201	$20.75 \pm 0.16$	$1.71 \pm 0.31$	$0.56 \pm 0.26$	$1.13 \pm 0.41$
554380301	$20.76 \pm 0.16$	$1.71 \pm 0.36$	$0.36 \pm 0.06$	$1.44 \pm 0.36$
PG1351+640				
205390301	$21.70 \pm 0.05$	$1.00 \pm 0.16$	$0.23 \pm 0.05$	$0.12 \pm 0.12$
556230201	$22.38 \pm 0.23$	$2.16 \pm 0.01$	$0.02 \pm 0.06$	$0.34 \pm 0.22$
PG1402+261				
400200101	$21.09 \pm 0.21$	$2.06 \pm 0.09$	$0.62 \pm 0.15$	$0.61 \pm 0.31$
400200201	$20.74 \pm 0.32$	$1.10 \pm 1.70$	$0.47 \pm 0.17$	$1.05 \pm 0.67$
PG1440+356				
5010101	$21.10 \pm 0.14$	$2.04 \pm 0.07$	$0.71 \pm 0.65$	$1.14 \pm 1.63$
5010201	$20.31 \pm 0.40$	$1.00 \pm 2.49$	$0.95 \pm 0.34$	-
5010301	$20.93 \pm 0.17$	$1.83 \pm 0.30$	$0.76 \pm 0.26$	$0.26 \pm 0.32$
107660201	$20.88 \pm 0.08$	$1.00 \pm 0.74$	$1.43 \pm 0.24$	$0.67 \pm 0.49$
Q0056-363				
102040701	$20.86 \pm 0.36$	$1.90 \pm 0.31$	$1.03 \pm 0.30$	$1.54 \pm 0.56$
205680101	$20.90 \pm 0.10$	$1.49 \pm 0.20$	$0.29 \pm 0.07$	$1.09 \pm 0.24$
401930101	$21.06 \pm 0.14$	$1.93 \pm 0.01$	$0.88 \pm 0.21$	$0.47 \pm 0.22$
RE1034+396				
109070101	$20.49 \pm 0.46$	$1.69 \pm 0.97$	$0.49 \pm 0.10$	$1.08 \pm 0.62$
506440101	$20.49 \pm 0.14$	$1.49 \pm 0.42$	$0.56 \pm 0.06$	$0.44 \pm 0.21$
561580201	$20.60 \pm 0.13$	$1.29 \pm 0.60$	$0.38 \pm 0.04$	$0.42 \pm 0.29$
655310101	$21.56 \pm 0.51$	$2.90 \pm 0.20$	$0.46 \pm 0.06$	-
655310201	$22.24 \pm 0.28$	$3.00 \pm 0.19$	$0.30 \pm 0.07$	-
675440101	$20.95 \pm 0.07$	$0.12 \pm 0.13$	$0.32 \pm 0.06$	-
675440201	$22.37 \pm 0.96$	$3.23 \pm 0.20$	$0.31 \pm 0.09$	$0.85 \pm 0.48$
675440301	$21.92 \pm 0.36$	$3.00 \pm 0.23$	$0.34 \pm 0.06$	-
UGC 3973				
103862101	$21.95 \pm 0.07$	$1.68 \pm 0.12$	$1.64 \pm 0.83$	$8.18 \pm 2.25$
400070201	$22.26 \pm 0.07$	$2.83 \pm 0.05$	$1.85 \pm 0.79$	$10.55 \pm 2.95$
400070301	$21.91 \pm 0.03$	$2.16 \pm 0.01$	$0.34 \pm 0.62$	$25.67 \pm 46.03$
400070401	$22.17 \pm 0.09$	$2.83 \pm 0.08$	$1.21 \pm 0.43$	$15.22 \pm 3.81$
502091001	$21.48 \pm 0.05$	$1.00 \pm 0.32$	$2.79 \pm 0.29$	$10.69 \pm 0.62$

Notes: '\*' denotes frozen values and '-' for last column denotes negligible reflection component.